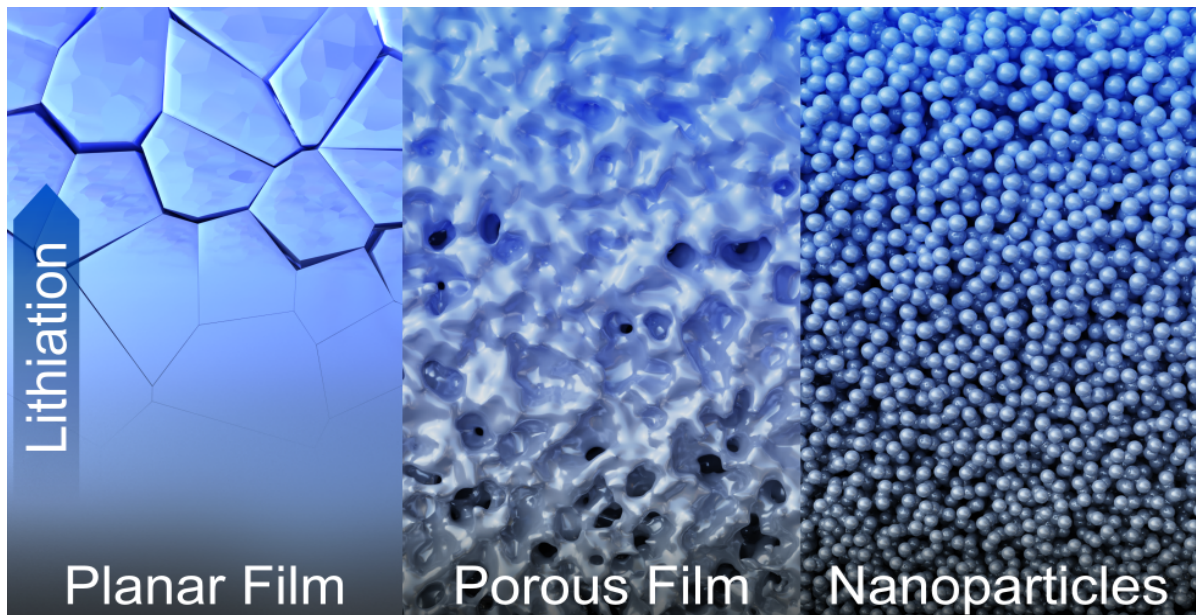


# Beyond Thin Films: Clarifying the Impact of $c\text{-Li}_{15}\text{Si}_4$ Formation in Thin Film, Nanoparticle, and Porous Si Electrodes

Jasper C. Woodard, W. Peter Kalisvaart,\* Sayed Youssef Sayed, Brian C. Olsen, Jillian M. Buriak\*

Department of Chemistry, University of Alberta, 11227 Saskatchewan Drive, Edmonton, AB T6G 2G2, Canada



\*Corresponding authors. Email addresses: [pkalisva@ualberta.ca](mailto:pkalisva@ualberta.ca) (P. Kalisvaart), [jburiak@ualberta.ca](mailto:jburiak@ualberta.ca) (J. Buriak)

## ABSTRACT

---

The formation of the  $c\text{-Li}_{15}\text{Si}_4$  phase has well established detrimental effects on the capacity retention of thin film silicon electrodes. However, the role of this crystalline phase with respect to the loss of capacity is somewhat ambiguous in nanoscale morphologies. In this work, three silicon-based morphologies are examined, including planar films, porous films, and silicon nanoparticle composites. The cycling conditions are used as the lever to induce, or not induce, formation of  $c\text{-Li}_{15}\text{Si}_4$  through application of constant-current (CC) or constant-current constant-voltage (CCCV) steps. In this manner, the role of this phase on capacity retention and Coulombic efficiency can be determined with few other convoluting factors such as alteration of the composition or morphology of the silicon electrodes themselves. The results here confirm that the  $c\text{-Li}_{15}\text{Si}_4$  phase increases the rate of capacity decay in planar films, but has no major effect on capacity retention in half cells based on porous silicon films or silicon nanoparticle composites, although this conclusion is nuanced. Besides using a constant-voltage step, formation of the  $c\text{-Li}_{15}\text{Si}_4$  phase is influenced by the dimensions of the Si material, the lithiation cut-off voltage and the electrolyte solvent. Porous Si films, which in this work comprise smaller primary Si particle sizes than the preformed Si nanoparticles, do not form  $c\text{-Li}_{15}\text{Si}_4$  at 50 mV, whereas Si nanoparticles form  $c\text{-Li}_{15}\text{Si}_4$  up to 80 mV. The solid-electrolyte interphase (SEI) formed from reaction of the  $c\text{-Li}_{15}\text{Si}_4$  with the carbonate-based electrolyte causes polarization in nanoparticle electrodes in particular, and lowers the average Coulombic efficiency in both nanoparticle and porous film silicon electrodes. A comparison of the cumulative irreversibilities due to SEI formation between different lithiation cut-off voltages in silicon nanoparticle electrodes confirmed the connection between higher SEI build up and formation of the  $c\text{-Li}_{15}\text{Si}_4$  phase. This work indicates that concerns about the  $c\text{-Li}_{15}\text{Si}_4$  phase in silicon nanoparticles and porous silicon electrodes should mainly focus on the stability of the SEI and a reduction of irreversible electrolyte reactions.

**Keywords:**

Silicon, porous silicon, films, lithium-ion batteries, anodes, nanoparticles, crystallization,  $\text{Li}_{15}\text{Si}_4$ , solid electrolyte interphase (SEI)

## INTRODUCTION

---

The transition from legacy fossil fuels to low-carbon energy sources requires efficient means of storing the energy captured from intermittent renewable sources.<sup>1</sup> Lithium-ion batteries currently underpin the market for portable electronics and electric vehicles, but their use for grid-scale integration remains limited. Further improvement of energy density (with respect to both mass and volume) is needed, and much attention is currently being directed to a wide range of materials for both the cathode and anode.<sup>2-4</sup> For anodes, one material of great interest is silicon that has a theoretical capacity of 3579 mAhg<sup>-1</sup>, based upon the formation of Li<sub>15</sub>Si<sub>4</sub>, which is almost an order of magnitude higher than that of graphite, the most commonly used anode in commercial batteries.<sup>5,6</sup> The capacity retention of silicon, however, is poor over several hundred cycles and thus far has seen only limited deployment.<sup>7,8</sup> The volume expansion of ~300% upon alloying silicon with lithium<sup>9</sup> results in pulverization of the material and formation of freshly cleaved Si surfaces, which react with the electrolyte, resulting in the formation of new solid electrolyte interphase (SEI).<sup>10</sup> Progressive fracturing and formation of SEI eventually result in disconnection of active Si, degrading the capacity.<sup>11-14</sup> Various strategies have been employed to mitigate fracture and disconnection, such as optimizing electrolyte composition,<sup>15-17</sup> including binders and conductive carbon additives,<sup>18-20</sup> as well as adding protective surface layers encapsulating the silicon.<sup>21-24</sup> Other strategies include changing the Si morphology to nanowires,<sup>25-27</sup> reducing the particle size to less than 100 nm,<sup>28-30</sup> and introducing porosity to better accommodate volume expansion.<sup>31-35</sup>

Targeted efforts to reduce fracture and improve capacity retention require an understanding of the alloying processes that occur as the voltage is lowered towards 0 V vs Li during lithiation and as the voltage is raised again during delithiation. In the first stages of electrochemical lithiation of crystalline Si, it is directly transformed to a highly lithiated amorphous silicon, *a*-Li<sub>*x*</sub>Si, typically at around 0.1 V vs Li.<sup>36,37</sup> The exact value of *x* is difficult to determine due to electrolyte decomposition taking place in conjunction with Li insertion into the Si, but the capacity associated with this transformation is >3000 mAh/g,<sup>38</sup> and the value of *x* has been reported as 3.4–3.5.<sup>37,39</sup> The terminal stage of lithiation that can be attained at room temperature is a metastable crystalline phase, where

$x = 3.75$  ( $c\text{-Li}_{15}\text{Si}_4$ ), typically at voltages below 50 mV vs Li.<sup>5,14</sup> The change in  $x$  specifically associated with this transition is around 0.2 as derived from galvanostatic intermittent titration technique (GITT),<sup>40</sup> and the final transition accounts for approximately 200 mAh/g of specific capacity.

Despite the relatively small additional capacity and expansion associated with its formation,  $c\text{-Li}_{15}\text{Si}_4$  has been linked to an increased loss of capacity in both silicon thin films,<sup>22,41</sup> and nanoparticles.<sup>30,42</sup> There are several reasons to suspect that lithiation of amorphous lithium silicide to the  $c\text{-Li}_{15}\text{Si}_4$  phase may lead to greater fracturing than lithiation ending in the amorphous phase. First, we cannot neglect that the transition from  $a\text{-Li}_x\text{Si}$  to  $c\text{-Li}_{3.75}\text{Si}$  increases the theoretical capacity by around 200 mAh/g to 3579 mAh/g. We would expect additional silicon expansion due to this increased capacity regardless of crystallization to the  $c\text{-Li}_{15}\text{Si}_4$  phase. Secondly, formation of  $c\text{-Li}_{15}\text{Si}_4$  creates a two-phase boundary between  $a\text{-Li}_x\text{Si}$  and  $\text{Li}_{15}\text{Si}_4$  during lithiation, and between  $c\text{-Li}_{15}\text{Si}_4$  and  $\text{Li}_y\text{Si}$ , where  $y$  is  $\sim 2$ , during delithiation.<sup>40</sup> Volume changes across a two-phase boundary are associated with increased stress, possibly leading to fracture and capacity loss in alloyed anodes generally,<sup>43</sup> and in silicon specifically.<sup>28,36,44</sup> Attempts to directly observe fracture in Si by in-situ TEM have instead overwhelmingly focussed on the initial transformation of  $c\text{-Si}$  to  $\text{Li}_x\text{Si}$ ,<sup>45</sup> and approaches to mitigate fracturing during this particular transformation by reducing the particle size or using amorphous rather than crystalline Si powder.<sup>28,45-47</sup>

The phase transformations associated with formation of  $c\text{-Li}_{15}\text{Si}_4$  involve a smaller change in the Li/Si ratio and hence a smaller volume change than the abrupt transformation from pristine silicon to Li-rich  $a\text{-Li}_x\text{Si}$ . However, the transition from  $c\text{-Si}$  to  $a\text{-Li}_x\text{Si}$  only happens in the first cycle and only for crystalline Si. There is a strong correlation between formation of the  $c\text{-Li}_{15}\text{Si}_4$  phase and capacity loss during long-term cycling. For instance, Xie et al. showed that the onset or acceleration of capacity degradation in 100 nm Si films on Cu coincides with the onset of  $c\text{-Li}_{15}\text{Si}_4$  formation.<sup>22</sup> Suppression of  $c\text{-Li}_{15}\text{Si}_4$  to improve capacity retention can be achieved by keeping the lithiation voltage above the onset of the  $c\text{-Li}_{15}\text{Si}_4$  transition, typically above 50 mV.<sup>14,48,49</sup> Higher charging rates will also prevent crystallization to  $c\text{-Li}_{15}\text{Si}_4$ , and at sufficiently high rates,  $c\text{-Li}_{15}\text{Si}_4$  will not form even if the cell is discharged to 0 V vs. Li.<sup>30,50,51</sup> The

use of a constant voltage (CV) step during lithiation, which is standard in commercial cells, also plays a large role in  $c\text{-Li}_{15}\text{Si}_4$  formation by increasing the time the electrode is exposed to low voltages.<sup>52</sup> However, there is a potential limit above which  $c\text{-Li}_{15}\text{Si}_4$  no longer forms using CCCV lithiation as well, as has been demonstrated by Sayed et al.<sup>23</sup> Recent work has taken advantage of stress-voltage coupling to suppress the  $c\text{-Li}_{15}\text{Si}_4$  phase, a process by which external stress lowers the lithiation voltage of the crystalline transition to  $c\text{-Li}_{15}\text{Si}_4$ , on the order of  $\sim 100\text{-}120$  mV/GPa as measured in-situ in thin silicon films.<sup>53</sup> Suppressing the transition voltage by 100 mV/GPa can be sufficient to lower the transition below 0 V vs. Li and avoid the appearance of the  $c\text{-Li}_{15}\text{Si}_4$  phase entirely. The stress-voltage coupling effect has been effectively harnessed to suppress the  $c\text{-Li}_{15}\text{Si}_4$  phase through the application of adhesive layers on thin films and capping layers on a variety of silicon morphologies,<sup>22,23,30,32,41,54</sup> as well as alloying silicon with inactive transition metals.<sup>22,42,55–58</sup> The hypothesis that alloying induces stress, thereby improving capacity retention by suppressing  $c\text{-Li}_{15}\text{Si}_4$ , has been applied to nano- and micron-sized silicon particle electrodes as well as thin films.<sup>55,59,60</sup> However, most, if not all previous studies that find a correlation between the suppression of  $c\text{-Li}_{15}\text{Si}_4$  formation and capacity retention achieve this suppression through material changes that are convoluted with other beneficial effects. For instance, a capping layer on top of a Si film can induce clamping, thereby preventing  $c\text{-Li}_{15}\text{Si}_4$  by aforementioned stress-voltage coupling, while also minimizing reactivity with the electrolyte.<sup>32,61–63</sup> Prolonged ball-milling of Si with Mo and W, for instance, increases the proportion of silicide intermetallic and allegedly induces stress, but this processing also reduces the grain size of Si,<sup>59,60</sup> rendering its distribution more homogeneous. Rather than suppressing  $c\text{-Li}_{15}\text{Si}_4$  formation by changing the electrode material, a test of the intrinsic effects of  $c\text{-Li}_{15}\text{Si}_4$  on capacity retention would, ideally, involve inducing or preventing its formation by adjusting only the experimental conditions while keeping the electrode material constant.

In the case of silicon nanoparticles, the role of particle size with regards to suppression of the  $c\text{-Li}_{15}\text{Si}_4$  phase and improving capacity retention has been more contentious. It is now well established that nanoparticles below 60 nm form the  $c\text{-Li}_{15}\text{Si}_4$  phase less readily than larger particles.<sup>30,48,64</sup> It is easy to confuse the fracture effects of the initial  $c\text{-Si} \rightarrow a\text{-Li}_x\text{Si}$  transition, which also diminish with decreasing size, and those

associated with formation of  $c\text{-Li}_{15}\text{Si}_4$ . However, the  $c\text{-Li}_{15}\text{Si}_4$  phase is still formed when fracture during the first lithiation is eliminated by using material below a critical size ( $\sim 150$  nm for  $c\text{-Si}$  nanoparticles and  $\sim 300$  nm for  $c\text{-Si}$  nanowires).<sup>28,47</sup> The multiple impacts of particle size complicate experiments to determine the intrinsic effects of the  $c\text{-Li}_{15}\text{Si}_4$  phase in silicon nanoparticles. For example, Gao et al. demonstrated that capacity loss with 120 nm Si nanoparticles was associated with formation of the  $\text{Li}_{15}\text{Si}_4$  phase at 0 mV vs. Li.<sup>30</sup> However, the difference in the quantity of  $c\text{-Li}_{15}\text{Si}_4$  formed was correlated with the use of fluoroethylene carbonate as an electrolyte additive, which is known to be beneficial in and of itself.<sup>65-67</sup> Smaller 60 nm silicon nanoparticles did not show any formation of the  $c\text{-Li}_{15}\text{Si}_4$  phase, even at 0 mV in ex-situ diffraction measurements on fully lithiated material.<sup>30</sup> It was assumed that the increased surface area compared to larger particles prevented the detection of the  $c\text{-Li}_{15}\text{Si}_4$  phase because of the enhanced reactivity of  $c\text{-Li}_{15}\text{Si}_4$  compared to  $a\text{-Li}_x\text{Si}$  as derived from static leakage current measurements.<sup>30</sup> Obrovac et al. also pointed out “polarization induced  $c\text{-Li}_{15}\text{Si}_4$  suppression” in the case of nanosized electrodes, which showed no formation of the  $c\text{-Li}_{15}\text{Si}_4$  phase near 0 V.<sup>8</sup> Schott et al. observed minimal loss of capacity retention associated with the appearance of  $c\text{-Li}_{15}\text{Si}_4$  in silicon/graphite electrodes, when using 5-10 wt% silicon relative to graphite in a blended electrode.<sup>48</sup> For the smallest nanoparticles, 30-50 nm, the influence of the  $c\text{-Li}_{15}\text{Si}_4$  phase on capacity retention, tested by comparing CC vs. CCCV lithiation, was minimal. In fact, CC cycling consistently showed worse capacity retention, irrespective of cut-off voltage and particle size, which means the CV step likely helps to reduce the effects of increasing polarization.<sup>48</sup>

In the present work, we attempt to establish a generalization of the role of the formation of the  $c\text{-Li}_{15}\text{Si}_4$  phase on capacity retention for three different Si morphologies: planar films, porous films, and commercially available Si nanoparticles. From the literature, the detrimental effect of  $c\text{-Li}_{15}\text{Si}_4$  is well-established for thin films, but its effect is less clear for nanoparticles of silicon and porous films. We confirm that the  $c\text{-Li}_{15}\text{Si}_4$  phase has a significant negative impact on capacity retention of planar films, but has only a small impact on capacity retention in silicon nanoparticles. The upper voltage limit for  $c\text{-Li}_{15}\text{Si}_4$  formation is  $\sim 80$  mV in Si nanoparticles and is dependent on size. We find evidence for higher reactivity of  $c\text{-Li}_{15}\text{Si}_4$  with the electrolyte compared to  $a\text{-Li}_x\text{Si}$

by comparing cumulative irreversibilities associated with SEI build-up in silicon nanoparticle electrodes with different lithiation cut-off voltages.

## **EXPERIMENTAL SECTION**

---

### **Materials**

Silicon nanoparticles (<100 nm, TEM), polyacrylic acid (PAA,  $M_v = 450,000$ ), lithium hydroxide (LiOH, reagent grade, >98%), 1 M LiPF<sub>6</sub> in 1:1 ethylene carbonate:diethyl carbonate (EC/DEC, 1/1 v/v%, battery grade), fluoroethylene carbonate (FEC, >99%, anhydrous), and lithium triflate (LiOTf, 99.995% trace metals basis) were purchased from SigmaAldrich. Dimethoxyethane (DME, Acros Organics, 99.5%, Max. 0.005% H<sub>2</sub>O, grade: extra dry over molecular sieves) was purchased from Fisher. DME was extracted from the stock bottle with a needle and syringe inside an Ar-filled glovebox and passed through a 0.2  $\mu$ m syringe filter prior to use. Super-P conductive additive was purchased from Timcal. The silicon nanoparticles were purchased as <100 nm from the manufacturer, but analysis with SEM imaging reveals that most particles are larger than 100 nm, with an average on the order of ~140 nm as shown in Figure S1.

### **Preparation of planar and porous Si films**

Stainless steel discs (MTI) of 0.5 mm thickness and 15.5 mm diameter were ultrasonically cleaned with dichloromethane, MilliQ water and isopropanol, and used as substrates. Elemental Si and co-deposited Si-Al films were prepared using an Orion 8 confocal sputtering system (AJA International) in sputter-up configuration. The deposition rate for Si was 0.22–0.28 A/s, at 75–100 W DC power with an Ar pressure of 4 mTorr. For the co-deposited films, the Al deposition rate was adjusted to yield compositions from 25 to 80 at% Al.

To obtain a porous Si film, the co-deposited films were annealed on a hotplate under Ar for 3 hours at 200–300 °C: For films with  $\leq 60$  at% Si, 200 °C was enough to induce crystallization of the Si and phase separation between the Si and Al as determined by XRD, Figure S2. For higher Si content, 300 °C was used. To dissolve the Al and obtain a porous Si film, the steel disks were immersed in 1 M (aq) KOH solution at room temperature for 1–2 minutes until hydrogen bubbling stopped. After dealloying, to remove residual KOH and water, the films were immersed in MilliQ water (twice) and

isopropanol for 5 minutes each, dried in a vacuum oven at 60 °C for 1 hour and cooled to room temperature while under vacuum. Stainless steel substrates were chosen instead of Cu foil,<sup>22,23</sup> because extensive delamination was observed during KOH immersion in the case of the Cu foil.

The nominal thickness of planar elemental Si films was 100 nm. The co-deposited films had identical areal Si as compared to the loading of the planar films, resulting in an as-deposited thickness greater than 100 nm, as calculated as follows:

$$t(\text{nm}) = 100 \left( 1 + \frac{1-x}{x} \times \frac{V_{m,Al}}{V_{m,Si}} \right) \quad (1)$$

with  $x$  as the atomic fraction of Si in the film, and  $V_{m,Al}$  and  $V_{m,Si}$  as the molar volumes of Al and Si, which are 10.00 and 12.06 cm<sup>3</sup>/mol, respectively. The film with 20 at% Si has an estimated as-deposited thickness of 432 nm according to the above formula.

Samples were weighed using a Mettler Toledo XP6U balance with a readability of 0.1 µg and a repeatability of 0.4 µg. The weight of a 100 nm planar Si film was typically around 40 µg. For the co-deposited films, the weight of Si was calculated assuming the composition of the as-deposited film was nominal. Using these weights and assuming complete removal of the Al during immersion in the aqueous KOH, the specific delithiation capacity in the first cycle was typically 3000–3200 mAh/g<sub>Si</sub> for the porous films.

### **Preparation of nanoparticle slurries**

LiPAA binder was prepared by titrating PAA in water with saturated LiOH (aq), creating an 8.5% LiPAA solution at pH ≈ 7.2. Slurries were prepared in an ambient atmosphere by combining as-purchased Si nanoparticles, Super-P and LiPAA in a 60:20:20 ratio and diluting with water (~160% mass of slurry). The solution was mixed in a planetary ball mill (Changsha Tianchuang Powder Technology Co.) at 500 rpm for 60 minutes total in a polyurethane vial using zirconia balls (~500% mass of slurry). The slurry was cast onto copper foil (battery grade, 10 µm) at a cast height of 100 µm and dried overnight at 120 °C under vacuum. Discs were punched with a diameter of 15 mm, then dried again at 120 °C under vacuum for 16 hours and brought directly under inert atmosphere.

### **Electrochemical measurements**

1 M LiPF<sub>6</sub> in EC/DEC (1/1 v/v%) with 10 wt% FEC additive and 1 M LiOTf in DME were used as electrolytes, with 45  $\mu$ L total used per cell. All cells were assembled under an argon atmosphere using 2032 coin cells with Li metal foil (MTI) counter electrodes and single layer polypropylene–polyethylene–polypropylene separators with a porosity of 39% (Celgard™ 2325). Cycle life testing was performed on an Arbin BT2000 battery testing system at 25 °C using two different lithiation protocols; constant-current (CC) and constant-current-constant-voltage (CCCV). In CC measurements, electrodes were lithiated to a low cut-off voltage using only a constant current. For the CCCV protocol, lithiation was held at the low cut-off voltage until a prescribed end-point. Delithiation was performed only using constant-current using the same specific current as for lithiation. Planar and porous films were cycled between 0.005 and 2 V vs. Li at a current density of 4  $\mu$ A/cm<sup>2</sup> for the first cycle and 10  $\mu$ A/cm<sup>2</sup> for subsequent cycles, corresponding to  $\sim$ 200 and 500 mA/g, respectively. Constant voltage steps were held for 10 hours in porous and planar films. For nanoparticle-based electrodes, cells were cycled between 1.5 V and various low cut-offs using 200 mA/g for the initial 3 cycles with 600 mA/g for all subsequent cycles. Constant voltage steps were held until reaching a current of 20 mA/g.

## **RESULTS AND DISCUSSION**

---

### **Planar and porous Si films**

Formation of *c*-Li<sub>15</sub>Si<sub>4</sub> is believed to have an intrinsically detrimental effect on capacity retention in planar Si thin films, and possibly other Si morphologies.<sup>22,23,30,41</sup> As a starting point to test this hypothesis, two cycle life testing protocols are needed in which, using otherwise identical electrodes, *c*-Li<sub>15</sub>Si<sub>4</sub> forms under one set of conditions but not the other. Even when using CCCV, *c*-Li<sub>15</sub>Si<sub>4</sub> does not form in the first 18 cycles in Si films on Cu.<sup>22</sup> Therefore, we hypothesized that for the planar 100 nm Si film on stainless steel, *c*-Li<sub>15</sub>Si<sub>4</sub> would not form during CC lithiation, and a comparison between CC and CCCV lithiation would enable us to test the intrinsic detrimental effect of *c*-Li<sub>15</sub>Si<sub>4</sub>, or lack thereof. *c*-Li<sub>15</sub>Si<sub>4</sub> is formed at a low lithiation potential of 5 mV,<sup>23,41</sup> but not at 25 mV,<sup>41</sup> or 50 mV vs. Li,<sup>23</sup> and therefore, a lithiation potential of 5 mV was chosen for the CV

step. The CV step was held for a fixed time of 10 hours rather than until a minimum current is reached,<sup>22,23,41</sup> to enable comparisons with porous Si films (vide infra) that have higher surface area and, as a result, a higher rate of Li consumption by electrolyte decomposition.

A comparison of the capacity retention with and without a CV step at 5 mV during lithiation and selected dQ/dV curves of the planar Si film is shown in Figure 1.

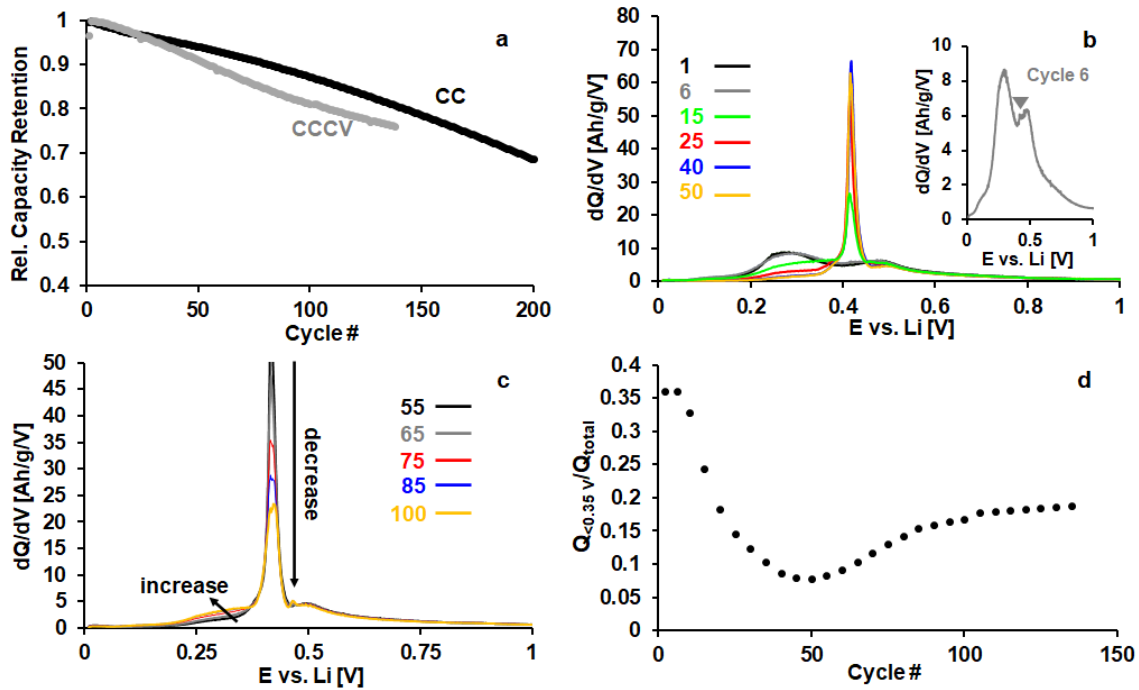


**Figure 1.** a): Comparison of the capacity retention between CC and CCCV protocols for the planar Si film, b) and c): dQ/dV curves for selected cycles using the CCCV protocol at 5 mV lithiation cut-off voltage, d): delithiation capacity below 0.35 V vs. Li as a fraction of total delithiation capacity vs. cycle number.

When plotting the capacity retention, the maximum capacity for each film is set to 1. The planar silicon film retains 69% of its maximum capacity after 200 CC cycles. Capacity degradation is clearly faster for the planar Si film when a CV step is applied compared to CC only, Figure 1a. Despite the long potential hold at 5 mV, no trace of  $c\text{-Li}_{15}\text{Si}_4$  was observed until the 6th cycle when the CCCV protocol was used. The characteristic peak of  $c\text{-Li}_{15}\text{Si}_4$  at  $\sim 0.42$  V then grows with each cycle and reaches a maximum around cycle 40. The height of the first broad peak at  $\sim 0.30$  V decreases in the same order, indicating an ever-larger fraction of  $c\text{-Li}_{15}\text{Si}_4$ , Figure 1b. Up to cycle 45, the

peak height at 0.42 V is more or less constant and starts to decrease after that point. A closer look at the  $dQ/dV$  curves beyond cycle 50 in Figure 1c reveals a clear inverse correlation between the height of the  $c\text{-Li}_{15}\text{Si}_4$  peak and that of the first amorphous peak centered at  $\sim 0.3$  V. Figure 1d is a plot of the delithiation capacity below 0.35 V, a potential between the peaks of the amorphous and crystalline phase, as a fraction of the total delithiation capacity as a function of cycle number. There is a minimum around cycle 50, where only  $\sim 8\%$  of the total capacity is extracted below 0.35 V, indicating that the fraction of the active material that forms  $c\text{-Li}_{15}\text{Si}_4$  is at its maximum there and declines afterwards. Around cycle 100, the amount of  $c\text{-Li}_{15}\text{Si}_4$  becomes approximately constant. For planar Si films on Cu, the ratio between  $c\text{-Li}_{15}\text{Si}_4$  peak area and the total delithiation capacity has been found to keep increasing, even as the total capacity rapidly declined.<sup>22,41</sup> The difference in the onset of the increase and decay of the  $c\text{-Li}_{15}\text{Si}_4$  peak area in different research works may be due to the choice of substrate, electrode design with and without adhesion and protective layers or length of the CV step, which was fixed at 10 hours here rather than using a lower current cut-off of 20 mA/g.<sup>22,23</sup> As shown in Figure S3, no trace of  $c\text{-Li}_{15}\text{Si}_4$  was found in the delithiation  $dQ/dV$  curves for any cycle, showing that for the planar film, formation of  $c\text{-Li}_{15}\text{Si}_4$  induced by the CV step at 5 mV does indeed lead to faster capacity degradation.

Porous Si films can be viewed as intermediate between planar films and nanoparticle electrodes. All of the active material is interconnected, as in any thin film, but the contact area with the rigid substrate is smaller compared to solid planar films. Due to their porosity, they share similarities with silicon nanoparticle electrodes, although they lack the supportive network of conductive carbon additive particles and binder that comprise such powder electrodes. SEM micrographs of porous silicon films prepared via annealing followed by dealloying are shown in Figure 2 for  $\text{Si}_{0.75}\text{Al}_{0.25}$  ( $x = 0.75$ ), and  $\text{Si}_{0.30}\text{Al}_{0.70}$  ( $x = 0.30$ ). At high Si content, the material appears as a planar film with pores up to 40 nm in diameter after dealloying. To contrast, the film with 70 at% Al,  $\text{Si}_{0.30}\text{Al}_{0.70}$ , is more of a porous aggregate of Si nanoparticles with a primary particle size of less than 50 nm. Intermediate compositions show a gradual progression between these two morphologies, as shown in Figure S4 in the Supplementary Materials. For  $\text{Si}_{0.20}\text{Al}_{0.80}$ , the morphology is virtually identical to  $\text{Si}_{0.30}\text{Al}_{0.70}$  with some deep cavities.

Elemental Si films deposited at room-temperature are usually amorphous<sup>22</sup> and the same is true for co-deposited films as shown in Figure S2. Subsequent annealing induces crystallization of the film and segregation of the Si and Al, resulting in the porous-slab and interconnected-particle morphologies shown in Figure 2 and Figure S4. Without the annealing step, films with more than 50% Si cannot be dealloyed in 1 M (aq) KOH. Instead, the films slowly delaminate without any visible bubbling to indicate dissolution of Al. Dealloying the as-deposited  $x = 0.30$  film results in a very different morphology as shown in Figure S5. Figure S6 shows that aside from XRD, crystallinity of Si is also easily deduced from the lithiation voltage profile. The first cycle was carried out in CC mode for all electrodes, to ensure all films had the same starting point when the CV step was initiated. Crystalline Si shows a long flat lithiation plateau at  $\sim 0.15$  V vs. Li, which is observed in the first cycle for the de-alloyed films, as per Figure S6b. Amorphous Si, on the other hand, shows a series of sloping plateaus, as observed for the planar Si film (Figure S6a) and for the de-alloyed films in the second cycle (Figure S6b).

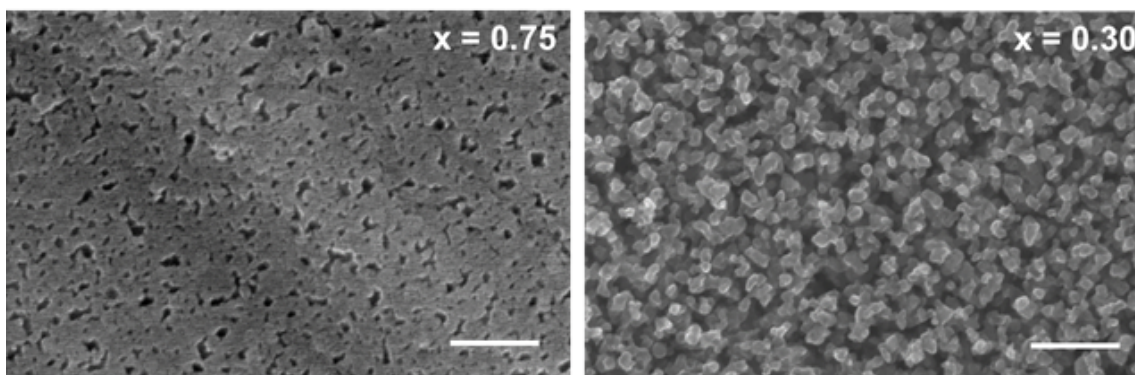


**Figure 2.** SEM micrographs of annealed  $\text{Si}_{0.75}\text{Al}_{0.25}$  ( $x = 0.75$ ), and  $\text{Si}_{0.30}\text{Al}_{0.70}$  ( $x = 0.30$ ) films after dealloying in 1 M (aq) KOH. Scale bars are 200 nm

Figure 3 depicts the relative capacity retention of the porous Si films with  $x = 0.75$  and  $x = 0.30$  with and without a CV step at 5 mV. Capacity retention in CC mode for all the porous Si films is shown in Figure S7. For  $x = 0.75$ , the capacity is slightly higher after 200 cycles using the CV step, but the electrode cycled in CC mode only degrades faster in the beginning, whereas the CV step causes a relatively faster degradation beyond cycle 50. For  $x = 0.30$  on the other hand, capacity retention is consistently *better* for CV as compared to CC and the difference in relative capacity retention becomes ever larger as cycling progresses. When the porous films are cycled

using only constant current (Figure S8), no sign of the  $c\text{-Li}_{15}\text{Si}_4$  phase is found for  $x = 0.30$ . A small peak at  $\sim 0.42$  V is visible in the first cycle for  $x = 0.75$ , never from the second cycle onwards. This is the first hint that the Si morphology has a big, perhaps decisive, influence on the formation of  $c\text{-Li}_{15}\text{Si}_4$ .

The  $dQ/dV$  curves for selected cycles of the  $x = 0.75$  and  $x = 0.30$  porous films using CCCV protocol are also shown in Figure 3. For  $x = 0.75$ , the amorphous peak around 0.30 V is lowest in the second cycle and therefore, the amount of  $c\text{-Li}_{15}\text{Si}_4$  is highest. The doublet structure of the  $c\text{-Li}_{15}\text{Si}_4$  peak has also been observed for C/Si multilayers and Si-Ti alloy films,<sup>22</sup> although the spacing between the peaks is much less than the 40 mV separation we observed in Si/C multilayer structures.<sup>23</sup> Although the  $c\text{-Li}_{15}\text{Si}_4$  peak *height* increases up to cycle 10, it also narrows and a broad peak around 0.30 V, characteristic of delithiation of amorphous  $\text{Li}_x\text{Si}$ , appears immediately after cycle 2 and starts to increase in height as well. The total capacity has in fact slightly degraded by cycle 10 (2%), so it appears that the tendency of the material to form  $c\text{-Li}_{15}\text{Si}_4$  diminishes with cycling. A similar picture emerges for  $x = 0.30$ , where the peak at 0.42 V reaches a maximum height around the 8th cycle and where the peak at 0.30 V increases in height between cycle 10 and cycle 50, despite severe degradation of the total capacity, indicating a diminished tendency towards formation of  $c\text{-Li}_{15}\text{Si}_4$  as well.

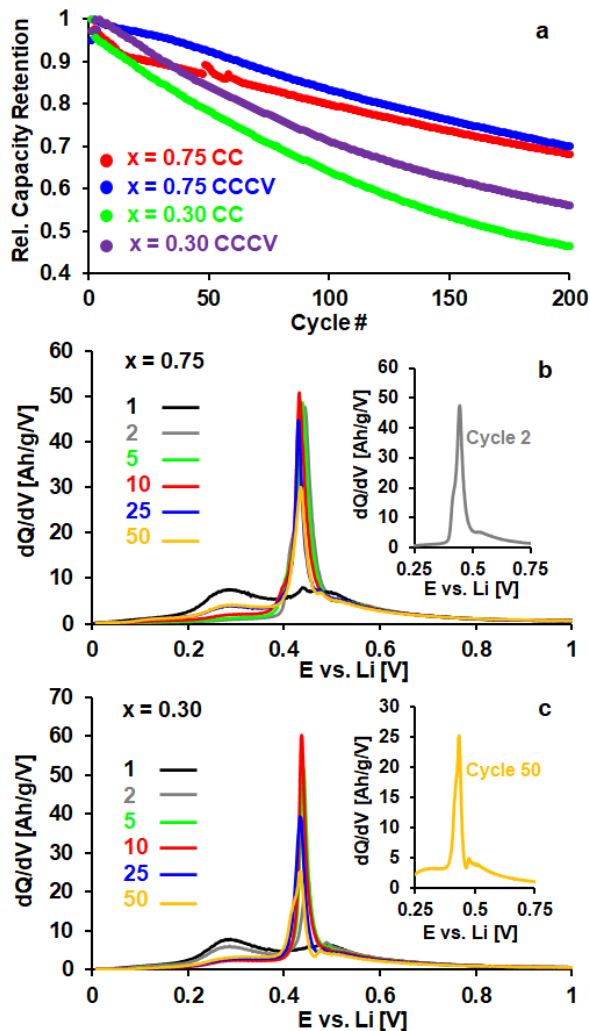


**Figure 3.** a): Relative capacity retention of  $x = 0.75$  and  $x = 0.30$  porous films comparing the CC and CCCV protocols at 5 mV lithiation cut-off voltage. b):  $dQ/dV$  curves for selected cycles for the  $x = 0.75$  porous film. c):  $dQ/dV$  curves for selected cycles for the  $x = 0.30$  porous film.

Formation of  $c$ - $\text{Li}_{15}\text{Si}_4$  is strongly dependent on stress exerted by a rigid substrate or inert interlayers present in the film.<sup>41,23</sup> Here too, we demonstrated that in a planar Si film, the quantity of  $c$ - $\text{Li}_{15}\text{Si}_4$  reaches its maximum around cycle 40, which is believed to be correlated in large part with delamination.<sup>22</sup> The porous films are much less constrained by the substrate, resulting in a reversal of the trend, with the amount of  $c$ - $\text{Li}_{15}\text{Si}_4$  diminishing with continued cycling. While part of the decrease is due to degradation of the total capacity, the (absolute) increase in the amorphous peak at 0.30 V indicates a reduced tendency to form  $c$ - $\text{Li}_{15}\text{Si}_4$ . There are two possible explanations for these observations for the porous silicon films: 1) fracture of the Si particle network, as

there are several studies showing an influence of particle size on the tendency to form  $c$ - $\text{Li}_{15}\text{Si}_4$ <sup>30,48</sup> and 2): a new source of mechanical stress, such as that exerted by the SEI. Since the SEI is formed during lithiation, it will constrain expansion of the lithiated silicon during cycling.

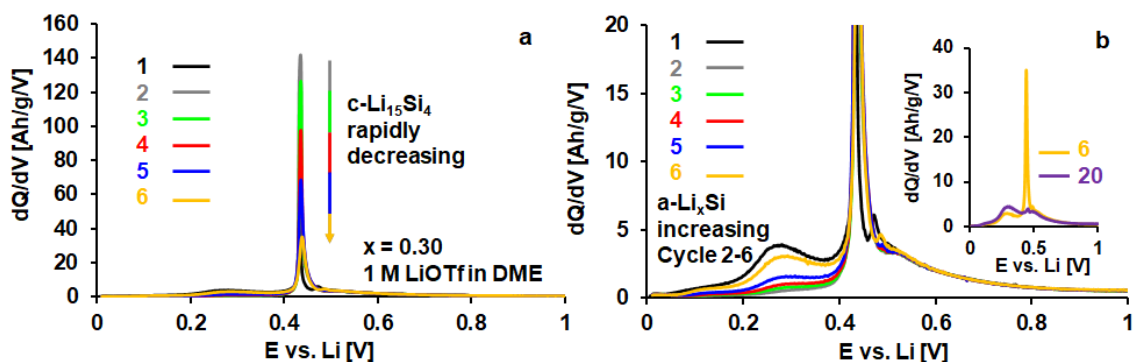


**Figure 4.** Delithiation  $dQ/dV$  curves of selected cycles of a porous  $x = 0.30$  film cycled in 1 M LiOTf in DME using CCCV. a): overview of  $dQ/dV$  curves showing the rapid decay in height of the  $c$ - $\text{Li}_{15}\text{Si}_4$  peak. b): Magnification of a) showing the evolution of the  $a$ - $\text{Li}_x\text{Si}$  peak. A comparison between cycle 6 and cycle 20 is shown in the inset of b).

The CE of the  $x = 0.30$  porous film is typically only around 95% in the early cycles and is lower for the CCCV protocol compared to CC as shown in Figure S9a. A thick SEI layer makes material fracture hard to quantify. The influence of particle size on  $c$ - $\text{Li}_{15}\text{Si}_4$  formation will be discussed, *vide infra*, by comparing with commercial Si nanoparticles. As an extreme example of the influence of SEI build-up, the results on cycling a  $x = 0.30$  film in 1 M LiOTf in dimethoxyethane (DME) are shown in Figure 4 for comparison. Although the initial CE is  $\sim 65\%$  for both carbonate-based and DME-based electrolyte, as shown in Figure S9b, the CE for the film cycled in 1 M LiOTf in DME remains consistently below 80%. A significant amount of  $c$ - $\text{Li}_{15}\text{Si}_4$  is also formed during the first CC cycle in DME-based electrolyte, contrary to the same composition cycled in carbonate-based electrolyte. This result is an indication that initially, the SEI formed in the DME-based electrolyte is less constraining than that formed in a carbonate-based electrolyte. As a result of the subsequent excessive SEI build-up, the  $c$ - $\text{Li}_{15}\text{Si}_4$  peak rapidly diminishes in the first 6 cycles, as shown on the left in Figure 4, while the amorphous peak at 0.30 V increases in the same order, as shown more clearly on the right in Figure 4. Although a difference in SEI thickness is hard to judge from an SEM

micrograph (see Figure S10), the much lower CE must mean a much thicker SEI was formed in the DME-based electrolyte. By the 20th cycle, the quantity of  $c\text{-Li}_{15}\text{Si}_4$  is negligible whereas the height of the amorphous peak has increased further as shown in the inset on the right of Figure 4.

### **Silicon nanoparticles**

~140 nm-diameter commercially available silicon nanoparticles with a 60 wt% loading in a slurry with Super P and LiPAA as conductive additive and binder, respectively, were used to prepare composite silicon nanoparticle electrodes with an average mass loading of 0.5-0.6 mg/cm<sup>2</sup>. We first examine cycling using a deep lithiation cut-off of 5 mV, terminating when the specific current reaches 20 mA/g. The CCCV protocol, terminating when a certain minimum specific current is reached, is usually implemented for safe practical charging of Li-ion batteries, and corresponds to lithiation of the anode active material.<sup>23,68</sup> Therefore, any (detrimental) effects of the CV step on the capacity retention of silicon nanoparticle electrodes are highly technologically relevant. We observe a sharp peak at 0.42 V vs. Li in the dQ/dV plot for delithiation (Figure 5a,b), again, characteristic of the  $c\text{-Li}_{15}\text{Si}_4$  phase, and corresponding to the plateau at the same voltage in Figure 5c,d. When the cell is held at the constant voltage of 5 mV, formation of  $c\text{-Li}_{15}\text{Si}_4$  persists until the 50th cycle (Figure 5a). However, without a CV step, the dQ/dV indicates delithiation from  $\text{Li}_{15}\text{Si}_4$  during the initial three cycles at 200 mA/g, but delithiation from amorphous lithium silicide as soon as the current is increased to 600 mA/g (Figure 5b). Despite the difference with respect to  $c\text{-Li}_{15}\text{Si}_4$  formation, the effect on absolute capacity and capacity retention is comparatively minor. The silicon anodes suffer capacity loss at roughly the same rates whether a CV step is included or not (Figure 5e). The maximum capacity is higher when a constant voltage step is used for silicon nanoparticles, reaching 3474 mAh/g and 3354 mAh/g for the CCCV and CC cells, respectively (Figure 5f). However, after more than ~20 cycles, both cells approach the same capacity and continue to decay at the same rates.

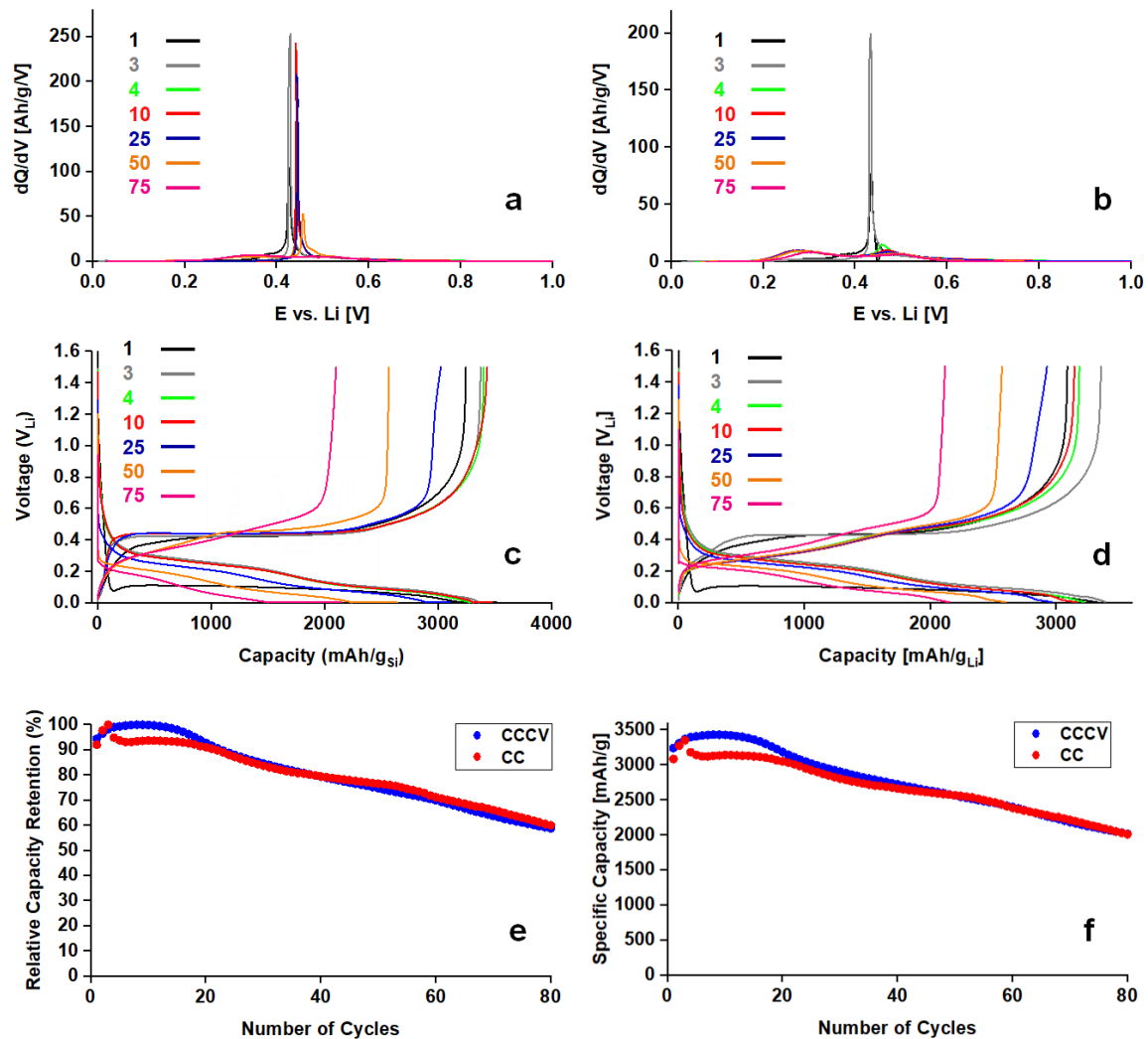


**Figure 5.** Delithiation  $dQ/dV$  curves (a,b), and charge/discharge curves (c,d) of silicon nanoparticle electrodes lithiated to a cut-off of 5 mV using CCCV (a,c) or CC (b,d) protocol. Plateaus in the delithiation curves correspond to peaks in the  $dQ/dV$  curves. All cells were delithiated to 1.5 mV vs Li using CC cycling only. Cycles 1-3 were performed at 200 mA/g, and all subsequent cycles at 600 mA/g. Cycle number is indicated in the accompanying legends. Relative (e) and absolute (f) capacity retention of the same two cells, with CC or CCCV cycling indicated in the legend.

50 mV is often considered the line above which  $c$ - $\text{Li}_{15}\text{Si}_4$  will not be formed in thin films,<sup>23,69</sup> although there are contrary examples with nanoparticles that show a dependence on size and charging rate.<sup>14,48</sup> Specifically, an increase of particle size above  $\sim 70$  nm and a decrease of charging rates are associated with more formation of the  $c$ - $\text{Li}_{15}\text{Si}_4$  phase.<sup>30,48,70</sup> Accordingly,  $dQ/dV$  reveals the presence of  $c$ - $\text{Li}_{15}\text{Si}_4$  at 50 mV in the silicon nanoparticle electrodes studied here when a constant voltage step is used

(Figure 6a). Without a constant voltage step, there is a small  $c\text{-Li}_{15}\text{Si}_4$  peak at 0.42 V during the first cycle, and none in subsequent cycles. Including a CV step at 50 mV does come with an increase in capacity, especially in early cycles, going from a maximum capacity of 2809 mAh/g for CC to 3322 mAh/g for the CCCV protocol. Comparisons of capacity retention with and without a constant voltage step are complicated by a fairly large gain in capacity during the first ten cycles (Figure 6e). Such a rise indicates incomplete lithiation in the early steps, the cause of which is not clear, but may be related to an improvement of electrolyte access resulting from the expansion and contraction of the Si. Nonetheless, after  $\sim 25$  cycles, both cells converge towards the same absolute capacity, and relative capacity loss is similar for both. The  $c\text{-Li}_{15}\text{Si}_4$  phase still continues to form in the CCCV cell after 25 cycles, but does disappear more quickly with a 50 mV cut-off than with a 5 mV cut-off.

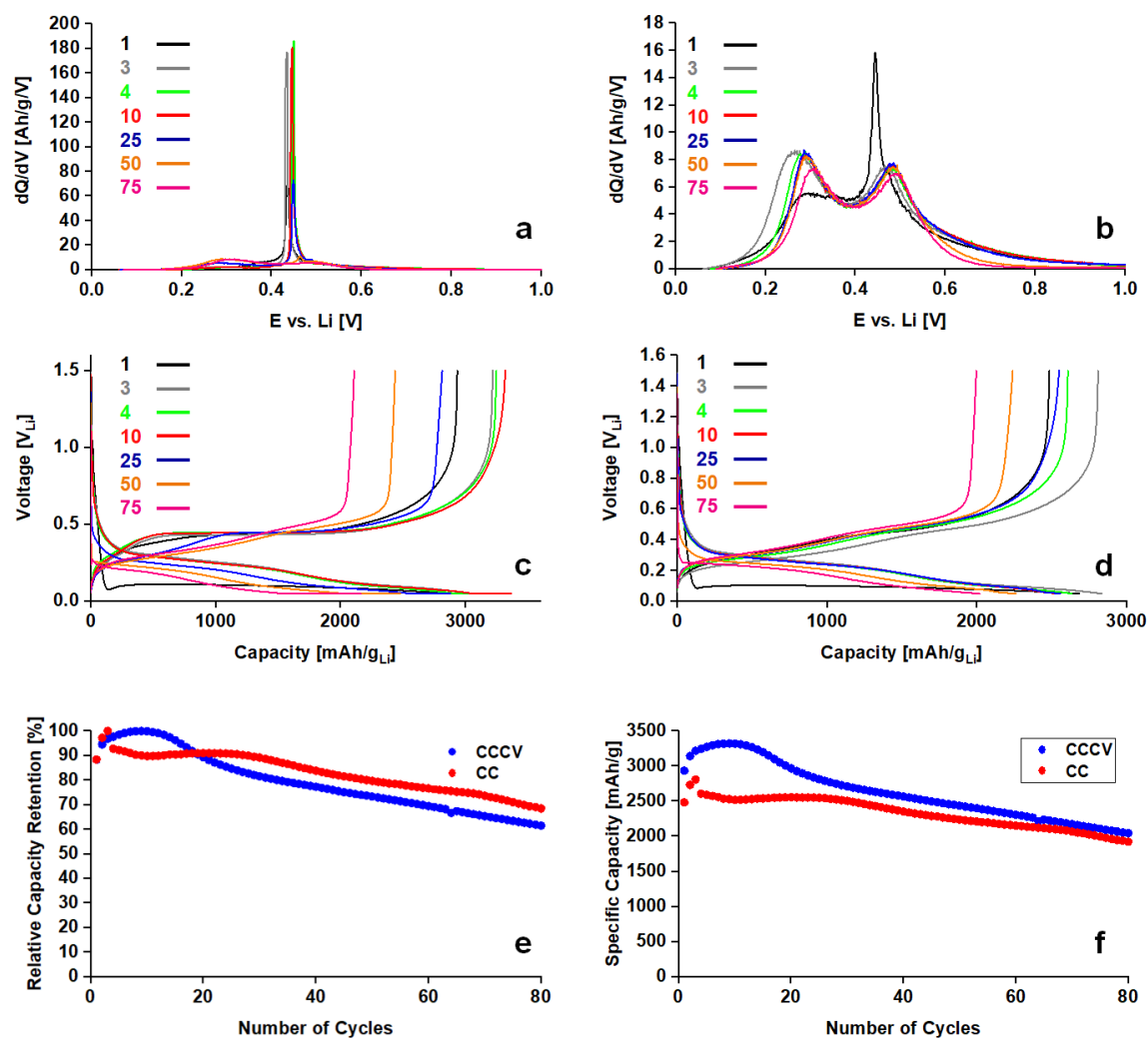


**Figure 6.** Delithiation  $dQ/dV$  curves (a,b), and charge/discharge curves (c,d) of silicon nanoparticle electrodes lithiated to a cut-off of 50 mV using CCCV (a,c) or CC (b,d) protocol. Plateaus in the delithiation curves correspond to peaks in the  $dQ/dV$  curves. All cells were delithiated to 1.5 V vs Li using CC cycling only. Cycles 1-3 were performed at 200 mA/g, and all subsequent cycles at 600 mA/g. Cycle number is indicated in the accompanying legends. Relative (e) and absolute (f) capacity retention of the same two cells, with CC or CCCV cycling indicated in the legend.

To help visualize the quantity of  $c$ - $\text{Li}_{15}\text{Si}_4$  that is formed in each cycle, as well as the differences between 5 mV and 50 mV cut-off, we plot the delithiation capacity before 0.35 V as a percentage of the total delithiation capacity (Figure 7). We chose this potential because it is past the peak potential of the first broad delithiation  $dQ/dV$  peak of the amorphous phase, and prior to the sharp peak characteristic of  $c$ - $\text{Li}_{15}\text{Si}_4$ . When the first phase transition falls between  $c$ - $\text{Li}_{15}\text{Si}_4$  and  $a$ - $\text{Li}_{12}\text{Si}$  at 0.42 V, there should be almost no capacity seen prior to 0.35 V. However, when the fully lithiated material remains

amorphous, the fraction of the total capacity prior to 0.35 V approaches 40%, as can be seen from Figure 7. Plotting delithiation in this manner helps to clarify the following results. First, we can observe the sharp contrast between cycling the 5 mV CC cells at 200 mA/g (cycles 1–3) and at 600 mA/g (cycles 4–80) (Figure 7a), in which  $c\text{-Li}_{15}\text{Si}_4$  is present and stable at the lower current, but disappears immediately when higher currents are applied. Using relative delithiation capacity <0.35 V, we can also clearly see that  $c\text{-Li}_{15}\text{Si}_4$  stops forming much earlier. With a cut-off of 5 mV and a CV step, the electrodes begin to derive more capacity from  $a\text{-Li}_x\text{Si}$  after ~40 cycles, with  $c\text{-Li}_{15}\text{Si}_4$  playing a minimal role after ~60 cycles, see Figure 7a. However, when the cut-off voltage is increased to 50 mV, the transition away from the  $c\text{-Li}_{15}\text{Si}_4$  phase starts and ends at ~20 and ~40 cycles, respectively (Figure 7b).

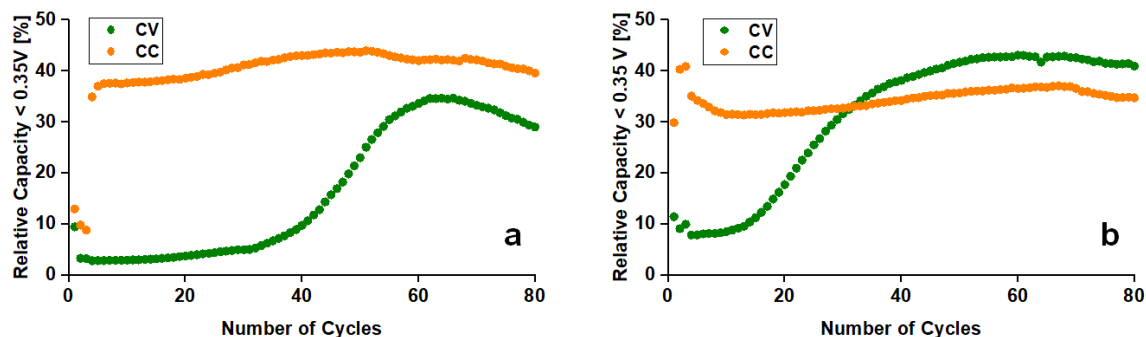


**Figure 7.** Percentage of delithiation capacity occurring below 0.35 V for silicon nanoparticle electrodes cycled to a lower cut-off of (a) 5 mV and (b) 50 mV vs Li for lithiation. CC and CCCV cycling are indicated in the accompanying legends. Cycles 1–3 were performed at 200 mA/g, and all subsequent cycles at 600 mA/g. All cells were delithiated to 1.5 V using CC protocol.

One important phenomenon largely absent in both the planar and porous silicon electrodes is increased polarization caused by an insulating SEI, which builds up on the nanoparticles and impedes lithium diffusion. Evidence of polarization can be seen in the rightward shift in the delithiation  $dQ/dV$ s with increasing cycles, most easily seen in Figure 8. Polarization is observed using both CC and CCCV cycling, but is more pronounced with the CCCV step. Cycle 75 in the 5 mV CCCV cell, Figure 8a, has a peak at ~0.34 V characteristic of delithiation from  $a\text{-Li}_x\text{Si}$ , while the corresponding peak in 5 mV CC cells has a maximum at ~0.3 V (Figure 8b). This shift indicates formation of a thicker SEI when a CV step is included, which impedes lithium diffusion.<sup>71</sup> Polarization

also has a visible effect using a cut-off voltage of 50 mV (Figure 8c,d). Both crystalline and amorphous delithiation peaks shift towards higher voltages, and by cycle 75 the peak maxima of  $a\text{-Li}_x\text{Si}$  are at 0.33 V and 0.31 V for CCCV and CC cycling respectively. Increased polarization also explains the gradual decline of the relative capacity below 0.35 V that is observed past cycle 65 in Figure 7a for CCCV cycling. The larger SEI build-up can also be observed by comparing coulombic efficiency with and without the constant voltage step (Figure 9). Initial coulombic efficiency is similar with and without a constant voltage step, but after increasing the rate to 600 mA/g, the coulombic efficiency remains lower with a constant voltage step as more reaction with the electrolyte occurs at low voltages.

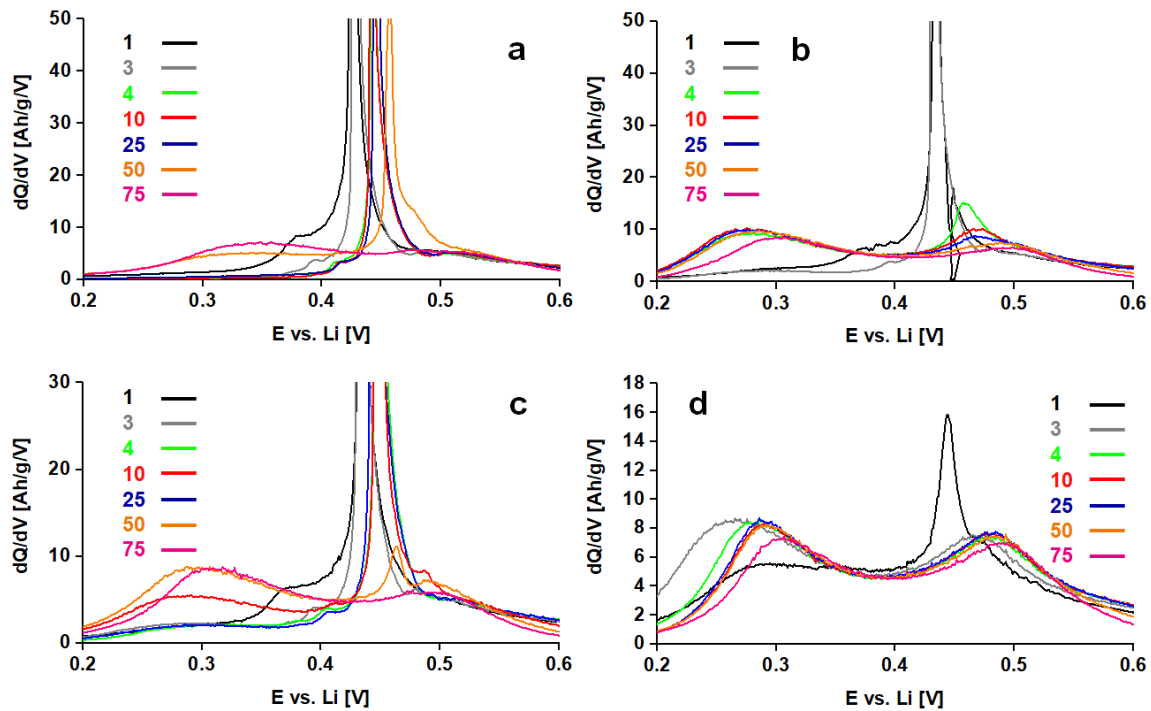


**Figure 8.** Close up of delithiation  $dQ/dV$  for silicon nanoparticle electrodes lithiated to 5 mV (a,b) and 50 mV (c,d) vs Li using CCCV (a,c) and CC (b,d) protocol. Cycle number is indicated in the accompanying legends. Cycles 1–3 were performed at 200 mA/g, and all subsequent cycles at 600 mA/g. All cells were delithiated to 1.5 V using CC protocol.

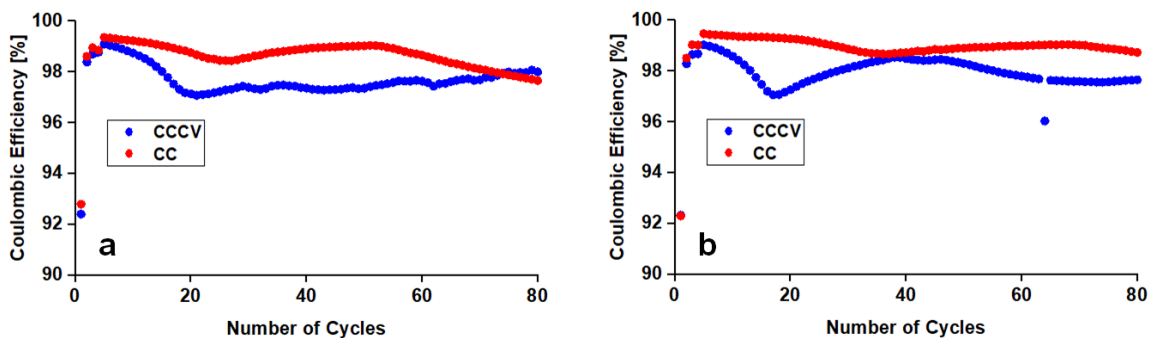


**Figure 9.** Coulombic efficiency of silicon nanoparticle electrodes cycled with a cut-off of (a) 5 mV and (b) 50 mV vs Li. CC or CCCV lithiation protocol is indicated in the legends. Cycles 1–3 were performed at 200 mA/g, and all subsequent cycles at 600 mA/g. All cells were delithiated to 1.5 V using CC protocol.

When we re-examine the question of how much impact  $c$ -Li<sub>15</sub>Si<sub>4</sub> formation has on capacity retention in silicon nanoparticles, the strongest evidence comes from a comparison of the cells cycled with a 5 mV lithiation cut-off in CC and CCCV modes. We find that both absolute capacity and capacity retention are very similar between the two protocols, despite the fact that crystallization stops after the 3rd cycle without a constant voltage step and persists until almost the 60th cycle, with a constant voltage step included. This result shows that formation of the  $c$ -Li<sub>15</sub>Si<sub>4</sub> phase plays a smaller role in capacity fade for silicon nanoparticle electrodes, as compared to planar films. The  $x = 0.30$  porous film and silicon nanoparticles are very similar in terms of Si morphology as well as capacity retention, despite the porous films not having binder or conductive additive, showing a possible influence of the smaller size of the Si particles in the porous film. To summarize, at 5 mV lithiation cut-off voltage, planar films, porous films and silicon nanoparticle electrodes behave similarly, only showing formation of  $c$ -Li<sub>15</sub>Si<sub>4</sub> under a CCCV protocol and remaining for the most part amorphous with a CC protocol. However, only the planar film showed a profoundly negative impact on capacity retention, due to formation of the  $c$ -Li<sub>15</sub>Si<sub>4</sub> phase.

The capacity of the silicon nanoparticle electrodes degrades most rapidly between cycles 15 and 25 (Figure 5e). Approximately half of the capacity degradation between cycles 10 and 60 occurs before the relative delithiation capacity below 0.35 V begins to decrease past cycle 30. From cycle 30 onwards, the degradation rate is more or less constant. Polarization begins to increase around cycle 25 as well, see Figure 8a,

coinciding with the decline in the amount of  $c\text{-Li}_{15}\text{Si}_4$  as evidenced by the decrease in relative delithiation capacity below 0.35 V. Therefore, whether SEI build-up also intrinsically affects formation of  $c\text{-Li}_{15}\text{Si}_4$  in silicon nanoparticles, as it did for the  $x = 0.30$  porous Si film cycled in DME-based electrolyte, is not clear as the increased polarization may be limiting the quantity of Li insertion. For the porous film, the  $c\text{-Li}_{15}\text{Si}_4$  peak declined very rapidly within the first 6 cycles. No increase in polarization was observed (Figure 4) and the decrease in  $c\text{-Li}_{15}\text{Si}_4$  is therefore likely caused by stress-voltage coupling. The capacity decay in the film was less than 5% over the same period, as seen in Figure S9. After 60 cycles, the 5 mV CCCV silicon nanoparticle cell had been reduced to 65% of its maximum capacity (Figure 5e), and the polarization increased (Figure 8a), at least partly due to SEI formation. At this point, the relative delithiation capacity below 0.35 V reaches its maximum, indicating that  $c\text{-Li}_{15}\text{Si}_4$  is no longer formed.

At 50 mV, the effects of the constant voltage step on capacity retention are harder to interpret because of a larger change in absolute capacity. However, a similar trend is observed as the rates of capacity decay trend towards the same levels over the long run (Figure 6e), even as the amount of  $c\text{-Li}_{15}\text{Si}_4$  continues to decline in the CCCV cells. The differences between silicon nanoparticles and porous silicon at 50 mV deserve some note, because while silicon nanoparticles do show formation of  $c\text{-Li}_{15}\text{Si}_4$  at 50 mV using a constant voltage step (Figure 6a), the  $x = 0.30$  porous silicon film remains amorphous (Figure S11). Previous studies have typically found that  $c\text{-Li}_{15}\text{Si}_4$  does not form above 50 mV in thin films<sup>5,23</sup> and nanoparticles smaller than  $\sim 70$  nm<sup>30,48</sup>. Therefore, our results can be viewed as further confirmation that particle size influences the tendency to form  $c\text{-Li}_{15}\text{Si}_4$ . The larger commercial silicon nanoparticles (around 140 nm on average, Figure S1) still fully crystallize at 50 mV CCCV, while the porous films, in which silicon has a size below  $\sim 50$  nm (Figure 2), do not.

Previous work has cited a wide range of voltages above which the  $c\text{-Li}_{15}\text{Si}_4$  phase does not form in silicon, including 50 mV,<sup>8,69,72</sup> 60 mV,<sup>30</sup> and 70 mV<sup>43</sup> for a wide variety of Si morphologies and lithiation rates. More recently, Tornheim et al. showed that formation of the  $c\text{-Li}_{15}\text{Si}_4$  phase in silicon nanoparticles can occur with cut-off voltages as high as 90 mV, but they only reported the first cycle.<sup>14</sup> As with Tornheim et

al., our work applies to silicon nanoparticles >100 nm in size in which the first cycle is run at ~200 mA/g or lower. As shown in Figure 10, we observe *c*-Li<sub>15</sub>Si<sub>4</sub> for >25 cycles at 60 mV, 10 cycles at 70 mV, and only on the first cycle for 80 mV, when a constant voltage step is included. There is no evidence of the *c*-Li<sub>15</sub>Si<sub>4</sub> phase at a lithiation cut-off of 90 mV. The relative delithiation capacity below 0.35 V is shown in Figure S12. The comparison of cycling with various cut-off voltages in Figure 11a can be used as another control for the effect of crystallization on capacity retention, although the differences in the absolute capacity probably play a role as well. The cells with a 5 mV cut-off do clearly show the most rapid loss of relative capacity, and there is a clear relationship between higher cut-off voltages and larger capacity retention at the end of 80 cycles. The nature of this capacity drop is uneven, however, with only minor differences in the rate of capacity loss after cycle 30. The results for 70, 80 and 90 mV in particular, show a very strong similarity. When we look at the absolute capacity in Figure 11b, we see that all cut-off voltages tend to converge at a similar absolute capacity in the long run. These findings are relevant for research into capacity limited anode cycling, which has been proposed as a potential compromise to mitigate capacity loss given the relatively high capacity of anodes compared to transition metal oxide cathodes for lithium-ion batteries.<sup>50,73</sup>

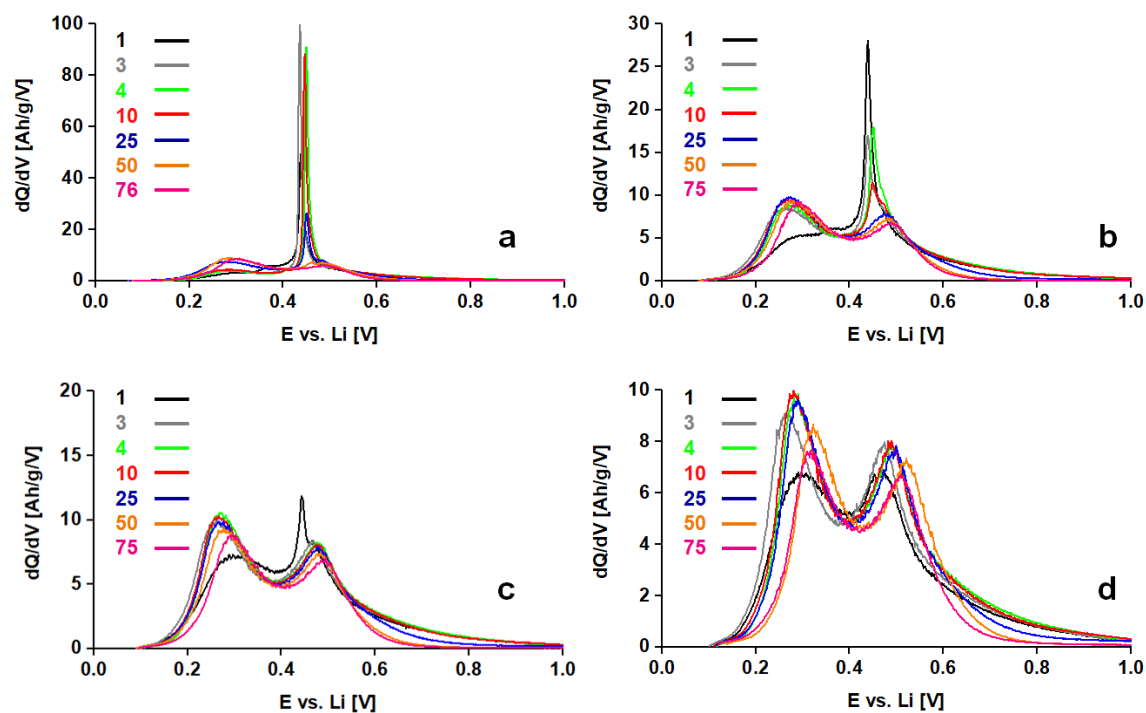


**Figure 10.** Delithiation  $dQ/dV$  for silicon nanoparticle electrodes cycled with a voltage cutoff of 60 mV (a), 70 mV (b), 80 mV (c), and 90 mV (d). Cycle number is indicated in the accompanying legends. All cycles used CCCV cycling, with a charging rate of 200 mA/g for cycles 1–3 and 600 mA/g for all subsequent cycles. All cells were delithiated to 1.5 V using CC protocol.

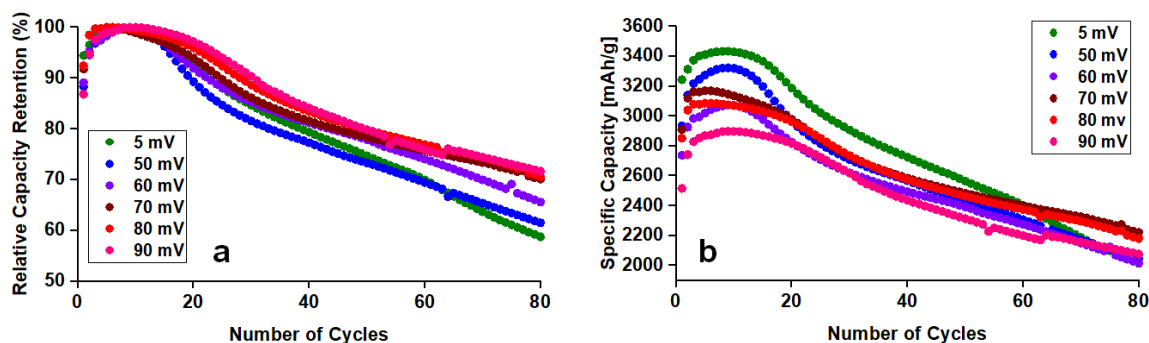


**Figure 11.** Absolute (a) and Relative (b) delithiation capacity of silicon nanoparticle electrodes cycled to cut-off voltages from 5–90 mV, as indicated in the accompanying legends. All cycles used CCCV cycling during lithiation, with a charging rate of 200 mA/g for cycles 1–3 and 600 mA/g for all subsequent cycles. All cells were delithiated to 1.5 V using CC protocol.

The biggest change in the amount of  $c\text{-Li}_{15}\text{Si}_4$  and how long  $c\text{-Li}_{15}\text{Si}_4$  formation persists, occurs between a 60 and 80 mV lithiation cut-off voltage (Figure 10a,c). The lower lithiation plateau of graphite is within the 60–80 mV vs. Li voltage interval,<sup>74,75</sup>

meaning that in graphite/Si blended electrodes,<sup>76</sup> Si will be exposed to potentials that are right on the cusp of inducing formation of *c*-Li<sub>15</sub>Si<sub>4</sub>, depending on size. As suggested by Gao et al., *c*-Li<sub>15</sub>Si<sub>4</sub> may be particularly reactive with the electrolyte,<sup>30</sup> which should result in lower coulombic efficiency when larger amounts of *c*-Li<sub>15</sub>Si<sub>4</sub> are formed.

Figure 12 shows a comparison of the cumulative losses due to SEI formation/electrolyte decomposition up to cycle 50, after which little to no *c*-Li<sub>15</sub>Si<sub>4</sub> was observed for 50 mV cut-off. Similar to our previous work,<sup>23</sup> a comparison of irreversible capacities resulting from SEI formation (RIC<sub>SEI</sub>) can be made by calculating the difference between lithiation capacity at cycle *n* + 1,  $Q_{n+1}^{\text{Lith}}$ , and delivered delithiation capacity of the previous cycle,  $Q_n^{\text{Delith}}$ , relative to the delithiation capacity at the *n*<sup>th</sup> cycle according to Equation 2.<sup>70</sup>

$$\sum \text{RIC}_{\text{SEI}} = \sum_{n=1}^N \frac{Q_{n+1}^{\text{Lith}} - Q_n^{\text{Delith}}}{Q_n^{\text{Delith}}} \quad (2)$$

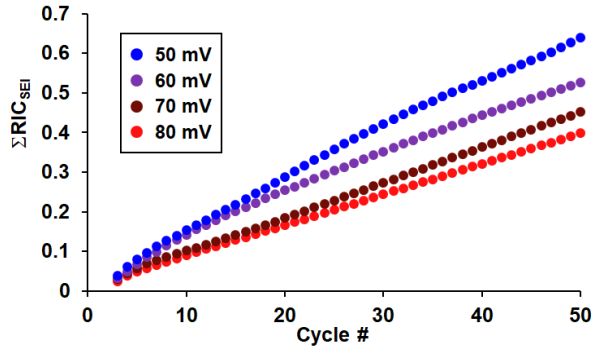


**Figure 12.** Cumulative irreversibilities due to electrolyte decomposition for silicon nanoparticle electrodes cycled with a lithiation voltage cutoff of 50–80 mV using CCCV protocol, as indicated in the legend. Cycles 1–3 were performed at a charging rate of 200 mA/g with subsequent cycles at 600 mA/g. All cells were delithiated to 1.5 V using CC protocol.

The advantage of using Equation 2 rather than the coulombic efficiency shown in Figure S13 is that it compares the lithiation capacity to the delithiation capacity in the previous cycle. Any lithiation in excess of the previous delithiation capacity can only be ascribed to electrolyte decomposition, especially when the delithiation capacity is itself degrading. There is a consistent downward trend in RIC<sub>SEI</sub> with increasing cut-off voltage, coinciding with a downward trend in amount and persistence of the *c*-Li<sub>15</sub>Si<sub>4</sub> phase. This comparison strongly suggests that *c*-Li<sub>15</sub>Si<sub>4</sub> indeed has higher reactivity

towards electrolyte decomposition compared to  $\alpha$ -Li<sub>x</sub>Si. This result is an important finding as small differences in the average coulombic efficiency can have a profound influence on the cycle life of balanced Li-ion full cells.<sup>43</sup>

## CONCLUSIONS

---

The intrinsic role of  $c$ -Li<sub>15</sub>Si<sub>4</sub> on capacity retention was examined by modulating the cycling conditions to either maximize or minimize its formation for three distinct Si morphologies: planar films, porous films and silicon nanoparticle electrodes. For all three morphologies, CC cycling minimized the quantity of  $c$ -Li<sub>15</sub>Si<sub>4</sub> formed, and was only observed for Si nanoparticles at a 5 mV lithiation cut-off and in the first cycle for the porous film with  $x = 0.75$ . Inclusion of a CV step at 5 mV vs. Li eventually induced the formation of  $c$ -Li<sub>15</sub>Si<sub>4</sub> in every case. For planar films, the quantity of  $c$ -Li<sub>15</sub>Si<sub>4</sub> first increases up to ~40 cycles, likely related to release of stress by partial delamination, and then decreases until ~80 cycles and remains constant thereafter. In porous Si films as well as Si nanoparticle electrodes, the amount of  $c$ -Li<sub>15</sub>Si<sub>4</sub> continuously decreases both absolutely and relatively with respect to the total delithiation capacity as cycling progresses. A causal and general link between the formation of the  $c$ -Li<sub>15</sub>Si<sub>4</sub> phase and capacity decay was not obvious, as capacity decayed at a similar rate for the CC and CCCV protocols in silicon nanoparticle electrodes and porous Si films. This observation is in contrast to the planar thin films, where it was found that  $c$ -Li<sub>15</sub>Si<sub>4</sub> is linked directly to an increased capacity loss, most likely due to delamination. While the  $c$ -Li<sub>15</sub>Si<sub>4</sub> phase is not associated with greater capacity loss in porous films and silicon nanoparticles, it does seem to be more reactive with the electrolyte. The larger buildup of SEI is observable both through larger polarization of the electrode and lower coulombic efficiencies using the CCCV protocol as compared to CC. Increasing the cut-off voltage in CCCV cycling resulted in both lower amounts of  $c$ -Li<sub>15</sub>Si<sub>4</sub> and lower cumulative irreversibilities due to electrolyte decomposition, confirming the increased reactivity of  $c$ -Li<sub>15</sub>Si<sub>4</sub> compared to an amorphous phase. Since there is no conclusive evidence for enhanced capacity degradation, the higher reactivity with the electrolyte should be regarded as the main reason for avoiding formation of the  $c$ -Li<sub>15</sub>Si<sub>4</sub> phase.

## ASSOCIATED CONTENT

---

### Supporting Information

Scanning electron microscopy (SEM) of nanoparticles, and planar and porous films, X-ray diffraction (XRD) of porous films and as deposited alloys, voltage vs capacity,  $dQ/dV$ , and capacity retention plots, as well as relative capacity <0.35 V, and Coulombic efficiency plots for silicon nanoparticle-based composite electrodes.

## AUTHOR INFORMATION

---

### Corresponding Authors

**W. Peter Kalisvaart** - Department of Chemistry, University of Alberta, 11227–Saskatchewan Drive, Edmonton, AB T6G 2G2, Canada; orcid.org/0000-0003-1228-906X  
Email: pkalisva@ualberta.ca

**Jillian M. Buriak** - Department of Chemistry, University of Alberta, 11227–Saskatchewan Drive, Edmonton, AB T6G 2G2, Canada; orcid.org/0000-0002-9567-4328  
Email: jburiak@ualberta.ca

### Authors

**Jasper C. Woodard** - Department of Chemistry, University of Alberta, 11227–Saskatchewan Drive, Edmonton, AB T6G 2G2, Canada; orcid.org/0000-0002-1870-3033

**Sayed Youssef Sayed** - Department of Chemistry, University of Alberta, 11227–Saskatchewan Drive, Edmonton, AB T6G 2G2, Canada; orcid.org/0000-0003-1575-676X

**Brian C. Olsen** - Department of Chemistry, University of Alberta, 11227–Saskatchewan Drive, Edmonton, AB T6G 2G2, Canada; orcid.org/0000-0001-9758-3641

## NOTES

---

The authors declare no competing financial interest.

## ACKNOWLEDGMENTS

---

This work was supported by Future Energy Systems of the University of Alberta (<https://futureenergysystems.ca>; grant numbers T12-P04), NSERC (grant number

RGPIN-2018-04294), Alberta Innovates Technology Futures (grant number AITF iCORE IC50-T1 G2013000198), Western Economic Diversification (WD, grant number 000014328), and the Canada Research Chairs program (CRC 207142). We thank the National Research Council (NRC) for use of laboratory facilities in the NRC-Edmonton site. We also thank the University of Alberta Centre for Nanofabrication (nanoFAB) for the use of their film deposition equipment.

## REFERENCES

---

- (1) Shaner, M. R.; Davis, S. J.; Lewis, N. S.; Caldeira, K. Geophysical Constraints on the Reliability of Solar and Wind Power in the United States. *Energy Environ. Sci.* **2018**, *11*, 914–925.
- (2) Manthiram, A. A Reflection on Lithium-Ion Battery Cathode Chemistry. *Nat. Commun.* **2020**, *11*, 1550.
- (3) Schmuck, R.; Wagner, R.; Hörpel, G.; Placke, T.; Winter, M. Performance and Cost of Materials for Lithium-Based Rechargeable Automotive Batteries. *Nat. Energy* **2018**, *3*, 267–278.
- (4) Li, F.; Xu, J.; Hou, Z.; Li, M.; Yang, R. Silicon Anodes for High-Performance Storage Devices: Structural Design, Material Compounding, Advances in Electrolytes and Binders. *ChemNanoMat* **2020**, *n/a*.
- (5) Obrovac, M. N.; Christensen, L. Structural Changes in Silicon Anodes During Lithium Insertion/Extraction. *Electrochem. Solid-State Lett.* **2004**, *7*, A93–A96.
- (6) Yao, K. P. C.; Okasinski, J. S.; Kalaga, K.; Shkrob, I. A.; Abraham, D. P. Quantifying Lithium Concentration Gradients in the Graphite Electrode of Li-Ion Cells Using *Operando* Energy Dispersive X-Ray Diffraction. *Energy Environ. Sci.* **2019**, *12*, 656–665.
- (7) Lindgren, F.; Rehnlund, D.; Pan, R.; Pettersson, J.; Younesi, R.; Xu, C.; Gustafsson, T.; Edström, K.; Nyholm, L. On the Capacity Losses Seen for Optimized

Nano-Si Composite Electrodes in Li-Metal Half-Cells. *Adv. Energy Mater.* **2019**, *9*, 1901608.

- (8) Obrovac, M. N. Si-Alloy Negative Electrodes for Li-Ion Batteries. *Current Opinion in Electrochemistry* **2018**, *9*, 8–17.
- (9) Beattie, S. D.; Larcher, D.; Morcrette, M.; Simon, B.; Tarascon, J.-M. Si Electrodes for Li-Ion Batteries—A New Way to Look at an Old Problem. *J. Electrochem. Soc.* **2008**, *155*, A158–A163.
- (10) Peled, E.; Menkin, S. Review—SEI: Past, Present and Future. *J. Electrochem. Soc.* **2017**, *164*, A1703–A1719.
- (11) Beaulieu, L. Y.; Eberman, K. W.; Turner, R. L.; Krause, L. J.; Dahn, J. R. Colossal Reversible Volume Changes in Lithium Alloys. *Electrochem. Solid-State Lett.* **2001**, *4*, A137–A140.
- (12) Rhodes, K.; Dudney, N.; Lara-Curzio, E.; Daniel, C. Understanding the Degradation of Silicon Electrodes for Lithium-Ion Batteries Using Acoustic Emission. *J. Electrochem. Soc.* **2010**, *157*, A1354.
- (13) Lee, Y. M.; Lee, J. Y.; Shim, H.-T.; Lee, J. K.; Park, J.-K. SEI Layer Formation on Amorphous Si Thin Electrode During Precycling. *J. Electrochem. Soc.* **2007**, *154*, A515.
- (14) Tornheim, A.; Trask, S. E.; Zhang, Z. Communication—Effect of Lower Cutoff Voltage on the 1st Cycle Performance of Silicon Electrodes. *J. Electrochem. Soc.* **2019**, *166*, A132.
- (15) Choi, N.-S.; Yew, K. H.; Lee, K. Y.; Sung, M.; Kim, H.; Kim, S.-S. Effect of Fluoroethylene Carbonate Additive on Interfacial Properties of Silicon Thin-Film Electrode. *Journal of Power Sources* **2006**, *161*, 1254–1259.
- (16) Jin, Y.; Kneusels, N.-J. H.; Magusin, P. C. M. M.; Kim, G.; Castillo-Martínez, E.; Marbella, L. E.; Kerber, R. N.; Howe, D. J.; Paul, S.; Liu, T.; Grey, C. P. Identifying the Structural Basis for the Increased Stability of the Solid Electrolyte Interphase Formed on

- Silicon with the Additive Fluoroethylene Carbonate. *J. Am. Chem. Soc.* **2017**, *139*, 14992–15004.
- (17) Schmiegel, J.-P.; Nölle, R.; Henschel, J.; Quach, L.; Nowak, S.; Winter, M.; Glorius, F.; Placke, T. Case Study of N-Carboxyanhydrides in Silicon-Based Lithium Ion Cells as a Guideline for Systematic Electrolyte Additive Research. *Cell Reports Physical Science* **2021**, 100327.
- (18) Jung, C.-H.; Kim, K.-H.; Hong, S.-H. Stable Silicon Anode for Lithium-Ion Batteries Through Covalent Bond Formation with a Binder via Esterification. *ACS Appl. Mater. Interfaces* **2019**, *11*, 26753–26763.
- (19) Higgins, T. M.; Park, S.-H.; King, P. J.; Zhang, C. (John); McEvoy, N.; Berner, N. C.; Daly, D.; Shmeliyov, A.; Khan, U.; Duesberg, G.; Nicolosi, V.; Coleman, J. N. A Commercial Conducting Polymer as Both Binder and Conductive Additive for Silicon Nanoparticle-Based Lithium-Ion Battery Negative Electrodes. *ACS Nano* **2016**, *10*, 3702–3713.
- (20) Rezaqita, A.; Hamid, R.; Schwarz, S.; Kronberger, H.; Trifonova, A. Conductive Additive for Si/Mesoporous Carbon Anode for Li-Ion Batteries: Commercial Graphite Vs Carbon Black C65. *ECS Trans.* **2015**, *66*, 17.
- (21) Reyes Jiménez, A.; Nölle, R.; Wagner, R.; Hüsker, J.; Kolek, M.; Schmuck, R.; Winter, M.; Placke, T. A Step Towards Understanding the Beneficial Influence of a LIPON-Based Artificial SEI on Silicon Thin Film Anodes in Lithium-Ion Batteries. *Nanoscale* **2018**, *10*, 2128–2137.
- (22) Xie, H.; Sayed, S. Y.; Kalisvaart, W. P.; Schaper, S. J.; Müller-Buschbaum, P.; Luber, E. J.; Olsen, B. C.; Haese, M.; Buriak, J. M. Adhesion and Surface Layers on Silicon Anodes Suppress Formation of  $c\text{-Li}_{3.75}\text{Si}$  and Solid-Electrolyte Interphase. *ACS Appl. Energy Mater.* **2020**, *3*, 1609–1616.
- (23) Sayed, S. Y.; Kalisvaart, W. P.; Olsen, B. C.; Luber, E. J.; Xie, H.; Buriak, J. M. Alternating Silicon and Carbon Multilayer-Structured Anodes Suppress Formation of the  $c\text{-Li}_{3.75}\text{Si}$  Phase. *Chem. Mater.* **2019**, *31*, 6578–6589.

- (24) Müller, V.; Bernhard, R.; Wegener, J.; Pfeiffer, J.; Rössler, S.; Scurtu, R.-G.; Memm, M.; Danzer, M. A.; Wohlfahrt-Mehrens, M. Evaluation of Scalable Porous Si-Rich Si/C Composites with Low Volume Expansion in Coin Cells to Prismatic Cell Formats. *Energy Technol.* *n/a*, 2000217.
- (25) Wu, H.; Cui, Y. Designing Nanostructured Si Anodes for High Energy Lithium Ion Batteries. *Nano Today* **2012**, *7*, 414–429.
- (26) Chan, C. K.; Peng, H.; Liu, G.; McIlwrath, K.; Zhang, X. F.; Huggins, R. A.; Cui, Y. High-Performance Lithium Battery Anodes Using Silicon Nanowires. *Nat. Nanotechnol.* **2008**, *3*, 31–35.
- (27) Lotfabad, E. M.; Kalisvaart, P.; Cui, K.; Kohandehghan, A.; Kupsta, M.; Olsen, B.; Mitlin, D. ALD TiO<sub>2</sub> Coated Silicon Nanowires for Lithium Ion Battery Anodes with Enhanced Cycling Stability and Coulombic Efficiency. *Phys. Chem. Chem. Phys.* **2013**, *15*, 13646–13657.
- (28) Liu, X. H.; Zhong, L.; Huang, S.; Mao, S. X.; Zhu, T.; Huang, J. Y. Size-Dependent Fracture of Silicon Nanoparticles During Lithiation. *ACS Nano* **2012**, *6*, 1522–1531.
- (29) Wu, S.; Yu, B.; Wu, Z.; Fang, S.; Shi, B.; Yang, J. Effect of Particle Size Distribution on the Electrochemical Performance of Micro-Sized Silicon-Based Negative Materials. *RSC Adv.* **2018**, *8*, 8544–8551.
- (30) Gao, H.; Xiao, L.; Plümel, I.; Xu, G.-L.; Ren, Y.; Zuo, X.; Liu, Y.; Schulz, C.; Wiggers, H.; Amine, K.; Chen, Z. Parasitic Reactions in Nanosized Silicon Anodes for Lithium-Ion Batteries. *Nano Lett.* **2017**, *17*, 1512–1519.
- (31) Li, X.; Gu, M.; Hu, S.; Kennard, R.; Yan, P.; Chen, X.; Wang, C.; Sailor, M. J.; Zhang, J.-G.; Liu, J. Mesoporous Silicon Sponge as an Anti-Pulverization Structure for High-Performance Lithium-Ion Battery Anodes. *Nat. Commun.* **2014**, *5*, 4105.

- (32) Lotfabad, E. M.; Kalisvaart, P.; Kohandehghan, A.; Cui, K.; Kupsta, M.; Farbod, B.; Mitlin, D. Si Nanotubes ALD Coated with TiO<sub>2</sub>, TiN or Al<sub>2</sub>O<sub>3</sub> as High Performance Lithium Ion Battery Anodes. *J. Mater. Chem. A* **2014**, *2*, 2504–2516.
- (33) Yang, Y.; Liu, S.; Bian, X.; Feng, J.; An, Y.; Yuan, C. Morphology- and Porosity-Tunable Synthesis of 3D Nanoporous SiGe Alloy as a High-Performance Lithium-Ion Battery Anode. *ACS Nano* **2018**, *12*, 2900–2908.
- (34) Yao, Y.; McDowell, M. T.; Ryu, I.; Wu, H.; Liu, N.; Hu, L.; Nix, W. D.; Cui, Y. Interconnected Silicon Hollow Nanospheres for Lithium-Ion Battery Anodes with Long Cycle Life. *Nano Lett.* **2011**, *11*, 2949–2954.
- (35) Chen, S.; Chen, Z.; Luo, Y.; Xia, M.; Cao, C. Silicon Hollow Sphere Anode with Enhanced Cycling Stability by a Template-Free Method. *Nanotechnology* **2017**, *28*, 165404.
- (36) McDowell, M. T.; Lee, S. W.; Nix, W. D.; Cui, Y. 25th Anniversary Article: Understanding the Lithiation of Silicon and Other Alloying Anodes for Lithium-Ion Batteries. *Adv. Mater.* **2013**, *25*, 4966–4985.
- (37) Ogata, K.; Salager, E.; Kerr, C. J.; Fraser, A. E.; Ducati, C.; Morris, A. J.; Hofmann, S.; Grey, C. P. Revealing Lithium–Silicide Phase Transformations in Nano-Structured Silicon-Based Lithium Ion Batteries via in Situ NMR Spectroscopy. *Nat. Commun.* **2014**, *5*, 3217.
- (38) Li, J.; Dahn, J. R. An In Situ X-Ray Diffraction Study of the Reaction of Li with Crystalline Si. *J. Electrochem. Soc.* **2007**, *154*, A156.
- (39) Key, B.; Bhattacharyya, R.; Morcrette, M.; Seznéc, V.; Tarascon, J.-M.; Grey, C. P. Real-Time NMR Investigations of Structural Changes in Silicon Electrodes for Lithium-Ion Batteries. *J. Am. Chem. Soc.* **2009**, *131*, 9239–9249.
- (40) Baggetto, L.; Oudenhoven, J. F. M.; van Dongen, T.; Klootwijk, J. H.; Mulder, M.; Niessen, R. A. H.; de Croon, M. H. J. M.; Notten, P. H. L. On the Electrochemistry

of an Anode Stack for All-Solid-State 3D-Integrated Batteries. *Journal of Power Sources* **2009**, *189*, 402–410.

(41) Iaboni, D. S. M.; Obrovac, M. N.  $\text{Li}_{15}\text{Si}_4$  Formation in Silicon Thin Film Negative Electrodes. *J. Electrochem. Soc.* **2015**, *163*, A255.

(42) Wang, Y.; Cao, S.; Kalinina, M.; Zheng, L.; Li, L.; Zhu, M.; Obrovac, M. N. Lithium Insertion in Nanostructured  $\text{Si}_{1-x}\text{Ti}_x$  Alloys. *J. Electrochem. Soc.* **2017**, *164*, A3006.

(43) Obrovac, M. N.; Chevrier, V. L. Alloy Negative Electrodes for Li-Ion Batteries. *Chem. Rev.* **2014**, *114*, 11444–11502.

(44) Zhao, K.; Pharr, M.; Wan, Q.; Wang, W. L.; Kaxiras, E.; Vlassak, J. J.; Suo, Z. Concurrent Reaction and Plasticity During Initial Lithiation of Crystalline Silicon in Lithium-Ion Batteries. *J. Electrochem. Soc.* **2011**, *159*, A238.

(45) McDowell, M. T.; Lee, S. W.; Harris, J. T.; Korgel, B. A.; Wang, C.; Nix, W. D.; Cui, Y. In Situ TEM of Two-Phase Lithiation of Amorphous Silicon Nanospheres. *Nano Lett.* **2013**, *13*, 758–764.

(46) Lee, S. W.; McDowell, M. T.; Berla, L. A.; Nix, W. D.; Cui, Y. Fracture of Crystalline Silicon Nanopillars During Electrochemical Lithium Insertion. *PNAS* **2012**, *109*, 4080–4085.

(47) Ryu, I.; Choi, J. W.; Cui, Y.; Nix, W. D. Size-Dependent Fracture of Si Nanowire Battery Anodes. *Journal of the Mechanics and Physics of Solids* **2011**, *59*, 1717–1730.

(48) Schott, T.; Robert, R.; Ulmann, P. A.; Lanz, P.; Zürcher, S.; Spahr, M. E.; Novák, P.; Trabesinger, S. Cycling Behavior of Silicon-Containing Graphite Electrodes, Part A: Effect of the Lithiation Protocol. *J. Phys. Chem. C* **2017**, *121*, 18423–18429.

(49) Obrovac, M. N.; Krause, L. J. Reversible Cycling of Crystalline Silicon Powder. *J. Electrochem. Soc.* **2006**, *154*, A103.

- (50) Erk, C.; Brezesinski, T.; Sommer, H.; Schneider, R.; Janek, J. Toward Silicon Anodes for Next-Generation Lithium Ion Batteries: A Comparative Performance Study of Various Polymer Binders and Silicon Nanopowders. *ACS Appl. Mater. Interfaces* **2013**, *5*, 7299–7307.
- (51) Misra, S.; Liu, N.; Nelson, J.; Hong, S. S.; Cui, Y.; Toney, M. F. In Situ X-Ray Diffraction Studies of (De)Lithiation Mechanism in Silicon Nanowire Anodes. *ACS Nano* **2012**, *6*, 5465–5473.
- (52) Chevrier, V. L.; Liu, L.; Le, D. B.; Lund, J.; Molla, B.; Reimer, K.; Krause, L. J.; Jensen, L. D.; Figgemeier, E.; Eberman, K. W. Evaluating Si-Based Materials for Li-Ion Batteries in Commercially Relevant Negative Electrodes. *J. Electrochem. Soc.* **2014**, *161*, A783.
- (53) Sethuraman, V. A.; Srinivasan, V.; Bower, A. F.; Guduru, P. R. In Situ Measurements of Stress-Potential Coupling in Lithiated Silicon. *J. Electrochem. Soc.* **2010**, *157*, A1253.
- (54) Bernard, P.; Alper, J. P.; Haon, C.; Herlin-Boime, N.; Chandesris, M. Electrochemical Analysis of Silicon Nanoparticle Lithiation – Effect of Crystallinity and Carbon Coating Quantity. *Journal of Power Sources* **2019**, *435*, 226769.
- (55) Du, Z.; Ellis, S. N.; Dunlap, R. A.; Obrovac, M. N. Ni<sub>x</sub>Si<sub>1-x</sub> Alloys Prepared by Mechanical Milling as Negative Electrode Materials for Lithium Ion Batteries. *J. Electrochem. Soc.* **2015**, *163*, A13.
- (56) Du, Z.; Hatchard, T. D.; Dunlap, R. A.; Obrovac, M. N. Combinatorial Investigations of Ni-Si Negative Electrode Materials for Li-Ion Batteries. *J. Electrochem. Soc.* **2015**, *162*, A1858.
- (57) Du, Z.; Liu, H.; Ellis, S. N.; Dunlap, R. A.; Zhu, M.; Obrovac, M. N. Electrochemistry of Cu<sub>x</sub>Si<sub>1-x</sub> Alloys in Li Cells. *J. Electrochem. Soc.* **2016**, *163*, A1275.
- (58) Liu, Y.; Sun, W.; Lan, X.; Hu, R.; Cui, J.; Liu, J.; Liu, J.; Zhang, Y.; Zhu, M. Adding Metal Carbides to Suppress the Crystalline Li<sub>15</sub>Si<sub>4</sub> Formation: A Route Toward

Cycling Durable Si-Based Anodes for Lithium-Ion Batteries. *ACS Appl. Mater. Interfaces* **2019**, *11*, 38727–38736.

(59) Liu, Y.; Bennett, J. C.; Obrovac, M. N. Ball Milled Si-W Alloys: Part II. Thermal Behavior and Performance in Li Cells. *J. Electrochem. Soc.* **2019**, *166*, A2791.

(60) Cao, S.; Gracious, S.; Bennett, J. C.; Obrovac, M. N. Synthesis, Lithium Insertion and Thermal Stability of Si–Mo Alloys. *J. Electrochem. Soc.* **2020**, *167*, 130531.

(61) Halim, M.; Kim, J. S.; Choi, J.-G.; Lee, J. K. Electrochemical Characterization of Carbon Coated Bundle-Type Silicon Nanorod for Anode Material in Lithium Ion Secondary Batteries. *Applied Surface Science* **2015**, *334*, 115–122.

(62) Kim, S. J.; Kargar, A.; Wang, D.; Graham, G. W.; Pan, X. Lithiation of Rutile TiO<sub>2</sub>-Coated Si NWs Observed by in Situ TEM. *Chem. Mater.* **2015**, *27*, 6929–6933.

(63) Shin, J.; Cho, E. Agglomeration Mechanism and a Protective Role of Al<sub>2</sub>O<sub>3</sub> for Prolonged Cycle Life of Si Anode in Lithium-Ion Batteries. *Chem. Mater.* **2018**, *30*, 3233–3243.

(64) Gan, C.; Zhang, C.; Wen, W.; Liu, Y.; Chen, J.; Xie, Q.; Luo, X. Enhancing Delithiation Reversibility of Li<sub>15</sub>Si<sub>4</sub> Alloy of Silicon Nanoparticles-Carbon/Graphite Anode Materials for Stable-Cycling Lithium Ion Batteries by Restricting the Silicon Particle Size. *ACS Appl. Mater. Interfaces* **2019**, *11*, 35809–35819.

(65) Etacheri, V.; Haik, O.; Goffer, Y.; Roberts, G. A.; Stefan, I. C.; Fasching, R.; Aurbach, D. Effect of Fluoroethylene Carbonate (FEC) on the Performance and Surface Chemistry of Si-Nanowire Li-Ion Battery Anodes. *Langmuir* **2012**, *28*, 965–976.

(66) Jaumann, T.; Balach, J.; Langklotz, U.; Sauchuk, V.; Fritsch, M.; Michaelis, A.; Telteviskij, V.; Mikhailova, D.; Oswald, S.; Klose, M.; Stephani, G.; Hauser, R.; Eckert, J.; Giebeler, L. Lifetime Vs. Rate Capability: Understanding the Role of FEC and VC in High-Energy Li-Ion Batteries with Nano-Silicon Anodes. *Energy Storage Materials* **2017**, *6*, 26–35.

- (67) Schroder, K.; Alvarado, J.; Yersak, T. A.; Li, J.; Dudney, N.; Webb, L. J.; Meng, Y. S.; Stevenson, K. J. The Effect of Fluoroethylene Carbonate as an Additive on the Solid Electrolyte Interphase on Silicon Lithium-Ion Electrodes. *Chem. Mater.* **2015**, *27*, 5531–5542.
- (68) Keil, P.; Jossen, A. Charging Protocols for Lithium-Ion Batteries and Their Impact on Cycle Life—An Experimental Study with Different 18650 High-Power Cells. *J. Energy Storage* **2016**, *6*, 125–141.
- (69) Bärmann, P.; Krueger, B.; Casino, S.; Winter, M.; Placke, T.; Wittstock, G. Impact of the Crystalline  $\text{Li}_{15}\text{Si}_4$  Phase on the Self-Discharge Mechanism of Silicon Negative Electrodes in Organic Electrolytes. *ACS Appl. Mater. Interfaces* **2020**.
- (70) Gauthier, M.; Mazouzi, D.; Reyter, D.; Lestriez, B.; Moreau, P.; Guyomard, D.; Roue, L. A Low-Cost and High Performance Ball-Milled Si-Based Negative Electrode for High-Energy Li-Ion Batteries. *Energy Env. Sci* **2013**, *6*, 2145–2155.
- (71) Schulze, M. C.; Carroll, G. M.; Martin, T. R.; Sanchez-Rivera, K.; Urias, F.; Neale, N. R. Hydrophobic Versus Hydrophilic Interfacial Coatings on Silicon Nanoparticles Teach Us How to Design the Solid Electrolyte Interphase in Silicon-Based Li-Ion Battery Anodes. *ACS Appl. Energy Mater.* **2021**.
- (72) Jiang, Y.; Offer, G.; Jiang, J.; Marinescu, M.; Wang, H. Voltage Hysteresis Model for Silicon Electrodes for Lithium Ion Batteries, Including Multi-Step Phase Transformations, Crystallization and Amorphization. *J. Electrochem. Soc.* **2020**, *167*, 130533.
- (73) Marinaro, M.; Weinberger, M.; Wohlfahrt-Mehrens, M. Toward Pre-Lithiated High Areal Capacity Silicon Anodes for Lithium-Ion Batteries. *Electrochimica Acta* **2016**, *206*, 99–107.
- (74) Zheng, T.; Dahn, J. R. The Effect of Turbostratic Disorder on the Staging Transitions in Lithium Intercalated Graphite. *Synth. Met.* **1995**, *73*, 1–7.

- (75) Zheng, T.; Reimers, J. N.; Dahn, J. R. Effect of Turbostratic Disorder in Graphitic Carbon Hosts on the Intercalation of Lithium. *Phys. Rev. B* **1995**, *51*, 734–741.
- (76) Jeschull, F.; Surace, Y.; Zürcher, S.; Lari, G.; Spahr, M. E.; Novák, P.; Trabesinger, S. Graphite Particle-Size Induced Morphological and Performance Changes of Graphite–Silicon Electrodes. *J. Electrochem. Soc.* **2020**, *167*, 100535.